Noise reduction for Offshore pile-driving of Monopiles

Master Thesis

M.B.M. Haarman

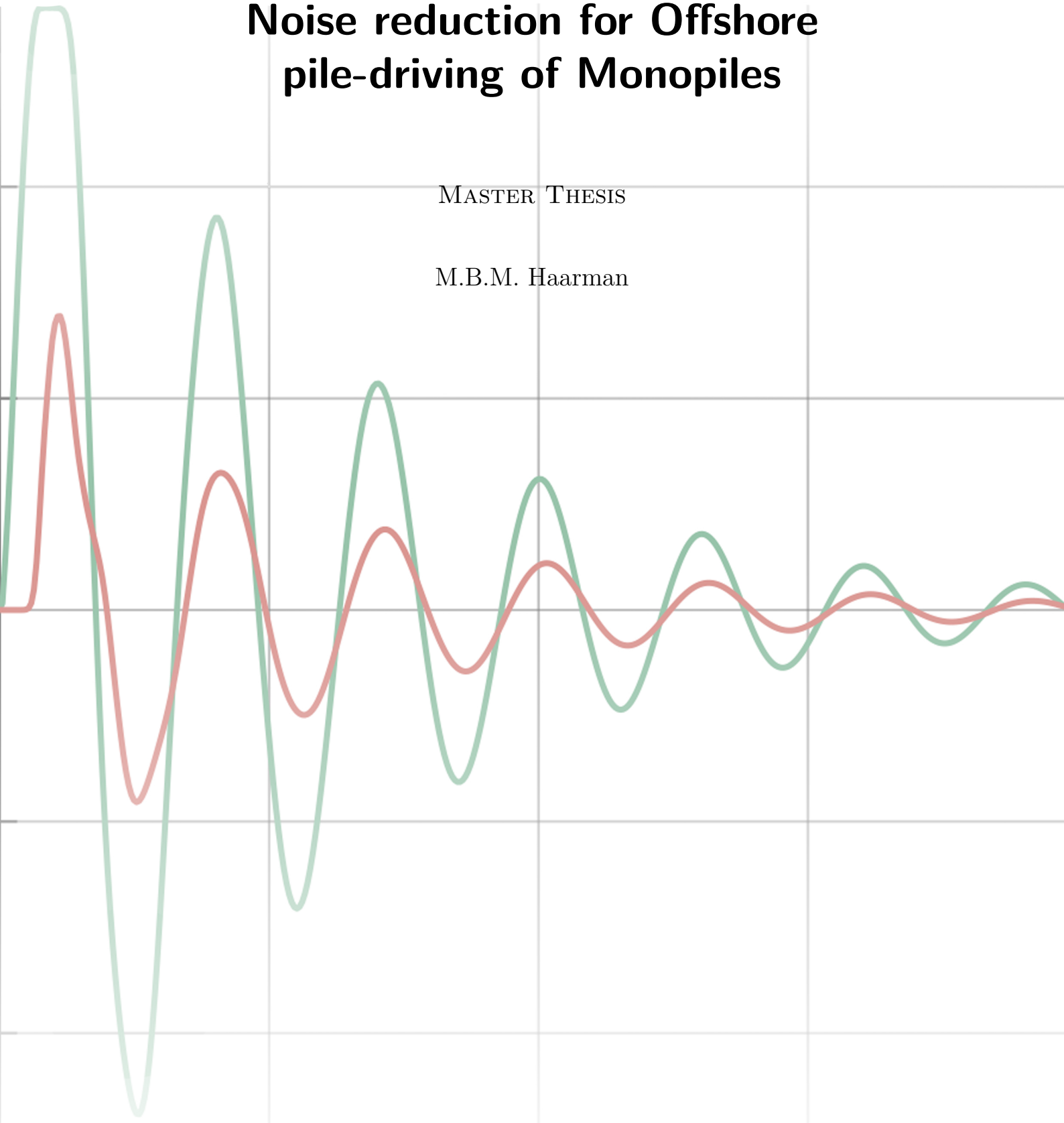

TWD
TEMPORARY WORKS DESIGN

TU Delft

Noise reduction for Offshore pile-driving of Monopiles

Master Thesis

For the degree of Master of Science in Structural Engineering at
Delft University of Technology

M.B.M. Haarman

June 20, 2017

Supervisors:

Prof.dr.ir. A.V. Metrikine (TU Delft)
Dr.ir. A. Tsouvalas (TU Delft)
Dr.ir.Drs. R. Braam (TU Delft)
Ir. J.B. van Wuijckhuijse (TWD)

Faculty of Civil Engineering and Geosciences · Delft University of Technology


TWD
TEMPORARY WORKS DESIGN BV


TUDelft

Abstract

The demand for offshore wind farms is developing rapidly due to the increased demand for renewable energy. Installation of foundation piles for offshore wind, however, are accompanied by a serious by-product which is the high underwater noise levels emitted during the pile-driving process. Current mitigation methods have proven to decrease the underwater noise emission, but these methods come at high costs. Moreover, these methods do not reduce the noise generation, but mitigate the noise that is already radiated into the water column. This study investigates a new concept, namely the reduction of noise at its source by altering the waves as they propagate downwards the pile. This is achieved by adding locally oscillators able to modify the shape of the wave front and thus influence the noise radiated into the water region.

The monopile is modelled schematically as a 1D rod affected by an impact load, and is coupled to a 2D model representing the pressure variations in the surrounding fluid. From an analysis in frequency domain on pressure intensity and on frequency response functions, it is found that the cut-off frequency of the fluid and the first eigenfrequency of the pile contain the most energy and have the most influence on the underwater noise levels. Therefore, the use of a Tuned Mass Damper (TMD) to reduce the influence of the first eigenfrequency and the use of additional stiffness to reduce the cut-off frequency are studied in this work. From these studies it appears that both methods flatten the wave front. However, adding stiffness increased the first eigenfrequency and decreased the periods of the deformations, which increased the noise levels in contrast with the expectations. The TMD, on the other hand, did reduce noise levels moderately. As an additonal study, an oscillator with damping is examined in its influence on noise reductions over a broader frequency spectrum. This method achieved higher reductions than the application of a TMD. Future studies have to quantify the effectiveness of the oscillators and can find an optimal combination between the three options. Additionally, a pile-driveability analysis has to be performed.

Table of Contents

List of Figures

Chapter 1

Introduction

1-1 Background information

All over the world, countries are exploring renewable energy resources for the preservation of our planet. As a result, the demand for energy from renewable resources generated by for example wind turbines, is increasing. Especially the offshore wind market shows a significant increase, since offshore wind parks generate energy more efficiently than onshore parks, due to less turbulence of offshore wind and higher speeds than onshore wind [1]. The Netherlands, for example, plan to expand their offshore wind generation capacity by an extra 3450 MW by 2023, in addition to the current 1000 MW [2]. This would mean an addition of 821 new wind turbines in the Dutch North Sea before 2023, generating 4.2 MW per turbine, assuming that it stays the same as the average wind turbine capacity in 2015 [3].

Although wind turbines offer an environmentally-friendly resource of energy, the installation of the foundation piles pollutes the sea with extreme impact noise under water due to the driving of the pile foundations into the seabed. In the North Sea, the wind turbine parks are usually installed on sandbanks, which are also the habitats of marine mammals and sea birds [4]. Additionally, the most popular foundation type of offshore wind turbines is the monopile. In 2015, 97% of the offshore wind turbines were supported by a monopile foundation [3]. During the installation phase, these monopiles are driven into the seabed using an impact hammer, which generates underwater noise, that can be noticed by animals miles away from the sound source.

1-1-1 Noise pollution

Marine mammals are especially affected by the impact noise pollution, since they use sound for communication, orientation and foraging. For example, behavioural changes

can be observed or mammal communication can be masked. When the mammals are too close to the source, Temporary Threshold Shift (TTS) or Permanent Threshold Shift (PTS) are possible injuries [5, 6]. A well-known scientific guidance with underwater noise exposure recommendations for all types of underwater noise came from Southall [7]. These recommendations are related to the hearing ranges of the marine mammals. In Table 1-1 the maximum exposure levels are presented for the two main groups of marine mammals, cetaceans (e.g. whales, dolphins and porpoises) and pinnipeds (e.g. seals), according to [7]. In this table, the Sound Exposure Level (SEL) represents the average level of noise to which the animal can be exposed during the whole hammering process and the peak pressure represents the maximum level of noise the animal can be exposed to. Both of these levels will be further explained in Chapter 3.

		SEL [dB re 1 μPa$^2 \cdot s$]	Peak pressure [dB re 1 μPa]
TTS	Cetaceans	183	224
	Pinnipeds	171	212
PTS	Cetaceans	198	230
	Pinnipeds	186	218

Table 1-1: Noise thresholds for marine mammals from Southall [7]

When comparing the data as presented in Table 1-1 with the current noise levels due to pile driving measured and presented in different papers (as summarised in Table 1-2), it can be seen that the noise levels caused by pile driving are around the thresholds set by Southall [7].

Location site	Diameter pile [m]	Length pile [m]	Hammer energy [kJ]	SEL [dB re 1 μPa$^2 \cdot s$]	SPL [dB re 1 μPa]
Anholt site, Baltic Sea [8]	5 m	45 m	350	184 dB @60 m 173 dB @750 m	207 dB @60 m 191.8 dB @750m
German North Sea [9]	6	55	800	181 dB @15 m 142 dB @1500m	206 dB @15 m 195 dB @140 m
Bard Offshore 1 [10]	3.35	85	1370	197.5 dB @10m 177.1 dB @1500m	No data available
Borkum West II [10]	2.5	34	800	164.5 dB @1500m 162.1 dB @2.9 km 135.6 dB @ 18.4 km	No data available
Blighbank a [11]	5	55	642	161 dB @750 m	No data available
Blighbank b [11]	5	63	839	164 dB @750 m	No data available

Table 1-2: Projects where noise is measured during construction

1-1-2 Regulations

Faijer [12] compares all the regulations of the countries surrounding the North Sea. Most of the countries focus on warning the mammals and extrude them from the construction site to avoid injury. The Netherlands is the only country with a regulation concerning the breeding season of the marine mammals. Untill a few years back, it was not allowed

to construct offshore wind farms between the 1st of January and the 1st of July when most animals are in the area [12]. In 2016, new guidelines were drafted for the new wind park in Borsele. For this park, the Dutch government dictates a noise level limitation, which differs per season and per amount of piles driven down into the seabed [13]. Neighbour country Germany limits the pile driving noise to a strict threshold level [12]: at 750 meters from the piling location the noise levels should remain below 160 dB SEL and 190 dB Sound Pressure Level (SPL, the maximum peak level during the process). Comparing this with the guidance of Southall, these values are well below the TTS and PTS thresholds of the mammals.

1-1-3 Mitigation methods

To reduce the underwater impact noise, different mitigation measures have been developed in the past few years. These methods prevent the noise from propagating through the water kilometres away and can be used to meet the thresholds set by authorities. In two papers [14] and [15], these methods are sorted in five categories and compared to each other:

1. Bubble Curtains
2. Pile Sleeves or Isolation Casings
3. Cofferdam
4. Hydro Sound Damper
5. Modification of the impact force

The first four methods reduce the noise entering the water column by using a shell. This shell creates an impedance gap using, for example air that reflects a part of the entering noise. However, the installation of these mitigation methods is often time consuming and therefore economically less profitable. Furthermore, with wind turbines constantly getting bigger using larger monopiles, these methods are becoming more and more difficult to apply. Another report, [14], studies prolonging of the impact force by use of a cushion on small diameter monopiles. This study shows that prolonging this impact lowers the noise levels, but also comes with a lowering of the effective impact force. Although this method is easier to use, it is not yet an effective method to reduce piling generated noise without affecting the piling time.

1-2 Problem description

Having said that, the following problem description is adopted:

> "Offshore pile driving generates impact noise levels that are harmful for marine life. To reduce this impact noise, there are currently two main solutions. One method is reduction of noise at the source, by prolonging the impact load over time. The downside of this method is that prolonging often goes together with a lowering of the impact force, which is required for effectively hammer the pile into the soil. A second method is mitigation of noise transferred into the surrounding media. Although it is possible to reach the approved threshold levels with mitigation measures, these methods are very inefficient in use and application."

1-3 Research statement

While the focus of current solutions lays on modification of the hammer process or on preventing the surrounding water from perturbation, this thesis will focus on modifying the structural vibration to reduce noise levels. The main research question therefore is:

> "Is it possible for the piling of offshore monopiles to reduce generated noise, measured in the surrounding water, by changing the dynamics of the pile itself?"

This statement is based on the assumption that reducing the noise generation close to the source will yield better mitigation results than the current solutions on the market. Moreover, the idea of changing the dynamics of the pile should lead to a simple and easy to install structure, which is economically attractive for the offshore wind market. The practical aspects of this modification, however, do not form part of this thesis.

1-4 Approach and Thesis outline

In order to find an answer to the main research question in this section the approach and thesis outline is described. First the monopile will be modelled, to understand what happens when the hammer hits the monopile and the physics of wave impact travelling through the pile. This will be presented in Chapter 2. Chapter 3 proposes a model for the acoustic medium, surrounding the pile. The two models will be coupled in Chapter 4 to develop a fully-coupled pile-water model. Before adjustments are made in order to reduce underwater noise levels, it is first of importance what the limitations of the model are, which is discussed in Chapter 5. Then the final model will help to understand how the shape of the waves excited in the monopile after each hammer blow the noise emission at a certain distance from the monopile and how noise levels can be best reduced with using the dynamic characteristics of oscillators, by means of an analysis in Chapter 6. In Chapter 7 these findings are implemented and the results are analysed.
The thesis ends with conclusions regarding the research statement and recommendations for future use of the results in Chapter 8.

Chapter 2

Wave propagation through monopiles

In the previous chapter, the problem description and goal of this thesis were described. To find an answer to the main question *"Is it possible to reduce generated noise during offshore pile driving, by changing the dynamics of the pile itself?"*, the first relevant key is to analyse the structural behaviour of a monopile after a hammer impact, i.e. waves propagating through the system.

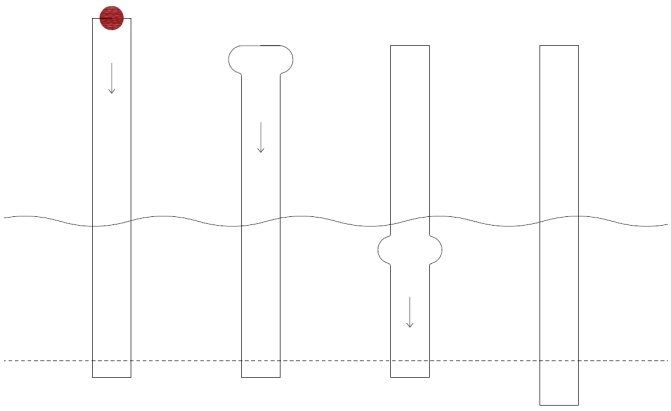

Figure 2-1: Wave propagation through a pile, during pile driving

Pile driving excites among others longitudinal waves, which in turn drive the pile into the ground sediment. Figure 2-1 presents how monopiles are driven into the seabed. After impact, a compressional wave travels down the pile. Each time the wave reflects from the bottom of the pile, the pile progresses into the soil. According to [16] and

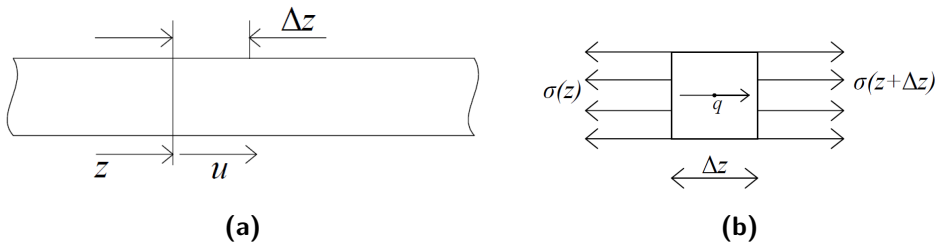

Figure 2-2: Schematization of a rod and its stresses (adopted from [18])

[17], the stress wave causes amongst others a displacement of the wall of a monopile in the axial direction and the radial direction due to Poisson's contraction. The radial displacement of the pile wall causes conical waves radiating from the pile into the water or the sediment. Hence, at each blow by the impact hammer, energy will be transferred into wave propagation. This chapter proposes several theories to describe travelling waves through a pile.

2-1 Longitudinal waves in thin long rods

2-1-1 Classical wave equation

A monopile can be simplified as a straight, prismatic rod, as shown in Figure 2-2a. It is assumed that the rod is under a dynamically varying stress $\sigma(z,t)$ and a body force $q(z,t)$ (see Figure 2-2b).

According to Newton's second law, the sum of the forces in z-direction is equal to the change of momentum in the body. Therefore:

$$-\sigma(z)A + \sigma(z+\Delta z)A + qA\Delta z = m\ddot{u} \tag{2-1}$$

$$-\sigma(z)A + \sigma(z+\Delta z)A + qA\Delta z = \rho A\Delta z\frac{\partial^2 u}{\partial t^2} \tag{2-2}$$

In this equation, m is the mass of the element, which is equal to $\rho A\Delta z$.
$\sigma(z+\Delta z)$ can be approximated using a Taylor expansion:

$$\sigma(z+\Delta z) \approx \sigma(z) + \frac{\partial\sigma}{\partial z}\Delta z \tag{2-3}$$

Equation 2-2 can now be reduced by substituting this expansion:

$$-\sigma(z)A + \sigma(zA) + \frac{\partial\sigma}{\partial z}\Delta zA + qA\Delta z = \rho A\Delta z\frac{\partial^2 u}{\partial t^2} \tag{2-4}$$

$$\frac{\partial\sigma}{\partial z}\Delta zA + qA\Delta z = \rho A\Delta z\frac{\partial^2 u}{\partial t^2} \tag{2-5}$$

$$\frac{\partial \sigma}{\partial z} + q = \rho \frac{\partial^2 u}{\partial t^2} \tag{2-6}$$

The stresses can be approximated by Hooke's law, assuming linear elasticity of the rod.

$$\sigma = E\varepsilon \tag{2-7}$$

$$\varepsilon = \frac{\partial u}{\partial z} \tag{2-8}$$

Substituting Equation 2-7 and 2-8, with E as the Young's Modulus and ε as the strain in the rod, into the equation of motion 2-6, we obtain:

$$\frac{\partial}{\partial z}\left(E\frac{\partial u}{\partial z}\right) + q = \rho \frac{\partial^2 u}{\partial t^2} \tag{2-9}$$

$$E\frac{\partial^2 u}{\partial z^2} + q = \rho \frac{\partial^2 u}{\partial t^2} \tag{2-10}$$

In Eq. (2-10) it is assumed that the Young's modulus is constant over the whole cross-section. When no external forces are applied, i.e. when $q(z,t)= 0$, the above equation simplifies to the wave equation:

$$c^2 \frac{\partial^2 u}{\partial z^2} - \frac{\partial^2 u}{\partial t^2} = 0 \tag{2-11}$$

$$\text{With} \quad c = \sqrt{\frac{E}{\rho}} \tag{2-12}$$

Constant c is also known as the wave speed.

2-1-2 Rayleigh-Love wave equation

The previous section described a simple model of a rod, without lateral inertia effects (also called the Poisson's effect). However, for this research insight in waves in radial direction is required to capture the dispersive character of waves travelling along large-diameter monopiles (for small-size monopiles under a usual hammer force, this dispersive character can be neglected). Therefore, the lateral inertia effects are introduced into the Rayleigh-Love wave equation. This equation of motion can be derived using the energy method, which is fully explained by Love [19] and Graff [20]. Its derivation can also be found in Appendix A. The new equation of motion, including lateral inertia and when assuming that there are no external forces, equals:

$$c^2 \frac{\partial^2 u}{\partial z^2} - \frac{\partial^2 u}{\partial t^2} + \frac{\nu^2 J}{A}\frac{\partial^2}{\partial t^2}\left(\frac{\partial^2 u}{\partial z^2}\right) = 0 \tag{2-13}$$

The components in Eq. (2-13) can be physically expressed as follows:

- $\rho\frac{\partial^2 u}{\partial t^2}$: The change of impulse or momentum. Impulse equals the mass of an element times the change of velocity of the element. The rate of change of impulse therefore is equal to the mass of an element times its acceleration, provided that the mass is constant. In the wave equation, this term describes the change of the wave over time at a particular location.
- $E\frac{\partial^2 u}{\partial z^2}$: Describes the change of stress along the z-axis.
- $\frac{\nu^2 J}{A}\frac{\partial^2}{\partial t^2}\left(\frac{\partial^2 u}{\partial z^2}\right)$: Lateral inertia effects, with Poisson's ratio ν and the derivation to both time and space. This term describes the effect of the lateral inertia onto the wave propagation.

An additional assumption is made in this step. The 1D model describes longitudinal deformations of a rod, which is not hollow due to its 1D characteristics. However, a monopile is hollow and this has its influence on the lateral inertia effects. Therefore, the hollow characteristics are incorporated into the polar moment of inertia J and into the cross-sectional area A.

2-1-3 Radial displacement

As explained previously, $u(z,t)$, in for example Eq. (2-13), represents a longitudinal displacement travelling along the z-axis of a rod. Due to the Poisson effect, the longitudinal displacement causes a rod to expand in radial direction. Using this relation, the radial displacement $w(z,t)$ can be described as follows:

$$\nu = -\frac{\varepsilon_\theta}{\varepsilon_z} \tag{2-14}$$

$$\text{Where: } \varepsilon_\theta = \frac{w(z,t)}{R} \tag{2-15}$$

$$\varepsilon_z = \frac{\partial u(z,t)}{\partial z} \tag{2-16}$$

$$\text{So that: } w(z,t) = -\nu R\frac{\partial u}{\partial z} \tag{2-17}$$

In Eq. (2-14) and (2-17), ν is the Poisson ratio of the rod's material and R represents the radius of a rod.

2-2 Thin shell theory

The previous section approaches the calculation of longitudinal waves using a simplified 1D method. This simple model provides information about the travelling waves (both

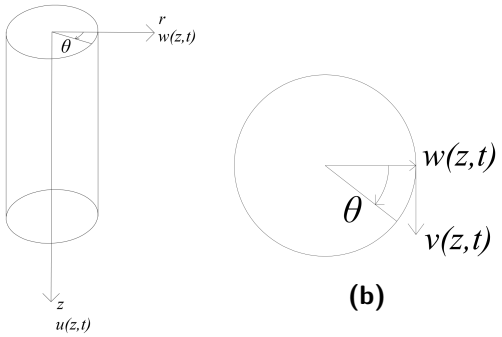

Figure 2-3: Geometry of cylindrical shell

longitudinal and radial) and their characteristics, but does not include bending of the walls of the rod itself. The thin shell theory, which is described in [21], includes these bending terms and describes a hollow cylinder under impact loading more accurately, in comparison with the classical one-dimensional wave equation. Eq. (2-18) to (2-20) present three equations for the longitudinal deformation $u(z,t)$, the radial deformation $w(z,t)$ and circumferential displacement v according to this thin shell theory. Figure 2-3 presents the corresponding geometry of the cylinder.

$$\frac{\partial^2 u}{\partial z^2} + \frac{1-\nu}{2R^2}\frac{\partial^2 u}{\partial \theta^2} + \frac{1+\nu}{2R}\frac{\partial^2 v}{\partial z \partial \theta} + \frac{\nu}{R}\frac{\partial w}{\partial z} - \frac{\ddot{u}}{c_p^2} = 0 \tag{2-18}$$

$$\frac{1+\nu}{2R}\frac{\partial^2 u}{\partial z \partial \theta} + \frac{1-\nu}{2}\frac{\partial v}{\partial z^2} + \frac{1}{R^2}\frac{\partial^2 v}{\partial \theta^2} + \frac{1}{R^2}\frac{\partial w}{\partial \theta} - \frac{\ddot{v}}{c_p^2} = 0 \tag{2-19}$$

$$\frac{\nu}{R}\frac{\partial u}{\partial z} + \frac{1}{R^2}\frac{\partial v}{\partial \theta} + \frac{w}{R^2} + \beta^2\left(R^2\frac{\partial^4 w}{\partial z^4} + 2\frac{\partial^4 w}{\partial z^2 \partial \theta^2} + \frac{1}{R^2}\frac{\partial^4 w}{\partial \theta^4}\right) + \frac{\ddot{w}}{c_p^2} - \frac{p_a(1-\nu^2)}{Eh} = 0 \tag{2-20}$$

Where $\beta^2 = \frac{h^2}{12R^2}$, R is the radius of a pile and h is equal to the wall thickness.

The thin shell theory states that a deformation in one direction depends to the other two directions. The above equations present this, since the terms $u(z,t)$, $v(z,t)$ and $w(z,t)$ appear at least one time in each equation. Besides this dependency, the deformations also depend on external pressure as this is included in Eq. (2-20). In this same equation also bending of the cylinder is included, with terms proportional to β.

It can be assumed that the torsional displacement ($v(z,t)$) is zero and the radial displacement is axisymmetric (hence, $\frac{\partial w}{\partial \theta} = 0$), when the impact load acts along the z-direction of the cylinder and the force is applied uniformly on the pile head. Under this assumption the system of equations of motion (Eq. (2-18) to (2-20)) is reduced to:

$$\frac{\partial^2 u}{\partial z^2} + \frac{\nu}{R}\frac{\partial w}{\partial z} - \frac{\ddot{u}}{c_p^2} = 0 \tag{2-21}$$

$$\frac{1-\nu}{2}\frac{\partial v}{\partial z^2} - \frac{\ddot{v}}{c_p^2} = 0 \tag{2-22}$$

$$\frac{\nu}{R}\frac{\partial u}{\partial z} + \frac{w}{R^2} + \beta^2 R^2 \frac{\partial^4 w}{\partial z^4} + \frac{\ddot{w}}{c_p^2} - \frac{p_a(1-\nu^2)}{Eh} = 0 \tag{2-23}$$

As presented in Eq. (2-21) to (2-23), the equation for $v(z,t)$ is decoupled from the equations for $u(z,t)$ and $w(z,t)$, i.e. 'torsional' modes are decoupled from axial-bending modes.
Eq. (2-23) can be simplified to Eq. (2-24a) and Eq. (2-24b) when the bending terms are much smaller than the inertia terms. However, in those cases in which the relationship between bending and inertia is unknown, Eq. (2-24a) and Eq. (2-24b) will yield to a certain error in the solution.

$$\frac{\partial^2 u}{\partial z^2} + \frac{\nu}{R}\frac{\partial w}{\partial z} - \frac{\ddot{u}}{c_p^2} = 0 \tag{2-24a}$$

$$\frac{\nu}{R}\frac{\partial u}{\partial z} + \frac{w}{R^2} + \frac{\ddot{w}}{c_p^2} - \frac{p_a(1-\nu^2)}{Eh} = 0 \tag{2-24b}$$

2-3 1D vs 2D

In Section 2-1 the 1D model was described and Section 2-2 described the thin shell theory. Both theories give the opportunity to calculate the longitudinal waves in a cylinder. The first method is a simple and classical approach, which describes a 1D rod and its longitudinal travelling waves. Radial displacement can then be described using the relation of Poisson between longitudinal and radial deformation. The second approach uses the thin shell theory, which is more complex but also more accurate. This section compares both methods and will end with a conclusion about which method is the best option for this research.

In order to make a well-informed choice, it is important to keep the goal of this thesis in mind and the aspects which are important to reach this goal.
The goal of this research is to reduce generated noise emission (the peak levels), by adjusting the pile's dynamical structure. Therefore the following aspects are of importance:

a) information on the evolution of the first wave travelling downwards through the pile

b) information on the evolution of the radial displacements

c) information of the dependency of the fluid pressure on the radial displacement

Besides these aspects, it is important to note that it is not in the scope of this thesis to find quantitative values for the reduction of the noise.

Both models will give information on the evolution of the first wave travelling downwards through the pile (Aspect a) and of the radial displacement (Aspect b). However, the 1D model will provide this information in a more clear and simpler way than the thin shell model and finding a solution will be more difficult in the thin shell model than for the 1D model, due to the higher number of derivatives and the coupling between the three different deformations. Simplification of the thin shell model, assuming that there is no rotational deformation (only two coupled deformations remain) and assuming that bending is small compared to inertia (neglecting the fourth derivatives in the equations), makes it easier to solve for longitudinal and radial deformation. However, neglecting the bending terms might lead to an inaccurate solution since it is not known whether or not these terms are indeed smaller than the inertia terms.

Information of the fluid pressure as described by Aspect c, cannot be found with either of these two models. It is necessary to model the fluid surrounding the pile separately, as will be done in Chapter 3. However, the thin shell theory does take the influence of this pressure on the (radial) deformation into account and the classical 1D model does not really. It is possible, though, to couple pressure and deformation in the 1D model, but for the sake of simplicity this will not be taken into account (yet) in this chapter, since we are mainly interested how a pile physically reacts on an impact force.

As stated previously, the purpose of this work is to examine qualitatively the effect of the shape of the waves in the pile to the pressure in the surrounding fluid medium. To meet this objective, a 1D model suffices; if one would like to examine the exact noise levels than a model based on the thin shell theory is required.

Aspect	**1D model**	**Thin shell model**
a	yes	yes
b	yes	yes
c	no[1]	no[1]
Accuracy	+	++
Simplicity	++	+ -

Table 2-1: Comparison of 1D model and Thin shell model

Table 2-1 gives a small overview of the comparison between both models. As seen, the 1D model and the thin shell model will provide information on all the important aspects needed to reach this research's goal, except for the last aspect. The thin shell theory will provide more accurate results, but since this is not necessary for the scope of this

[1] Although both models do not give information of the fluid pressure, the dependency of the fluid pressure on the deformation of the pile is taken into account in the Thin shell model. This is not the case in the classical 1D model, but it is possible to do as will be done later in this thesis in Chapter 4.

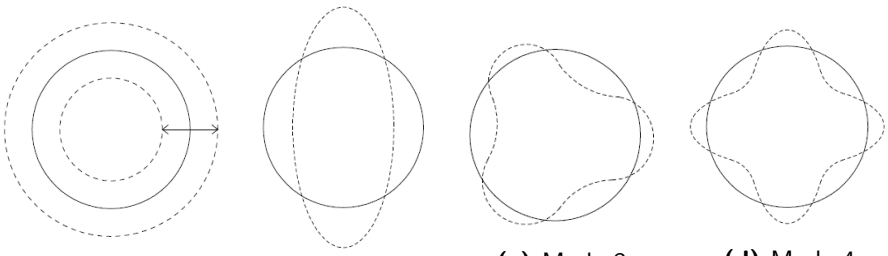

(a) Mode 1 **(b)** Mode 2 **(c)** Mode 3 **(d)** Mode 4

Figure 2-4: Different modes around the z-axis of a monopile

thesis, this aspect is left out in the final choice. Simplicity is now the remaining factor, and therefore the 1D model will be used for further work in this thesis.

2-4 Assumptions

Both of the methods described in Section 2-1 and Section 2-2 present a simple model of waves travelling in a pile, assuming that impact loading is exact in line with the z-axis of the pile. This would mean that the hammer force excites a monopile equally at every point of the pile's head and therefore it is only possible to excite the first mode (see Figure 2-4a).

There is, however, a large possibility that the force is applied eccentric [1]:

1. the hammer might have a small inclination
2. the monopile itself might not be standing straight
3. a combination of both is present

Assuming that one aims to hammer the pile exactly vertical into the seabed, these three options causing a small inclination of either the pile or the hammer or both, leads to a small horizontal force acting on the monopile. This horizontal force causes the monopile to vibrate not only in the first mode, but also in other higher modes as presented in Figure 2-4. In other words, the pile would not only be excited in the cylindrically symmetric mode (i.e. n=0), but also in the other modes as visualized in the above figure and downwards travelling waves will also depend on θ, as in Eq. (2-18) to (2-20). In this thesis it is assumed that there is no inclination of the impact force. Although this assumption will not give exact values for the deformation of a pile, the simplification will provide the information needed for this research.

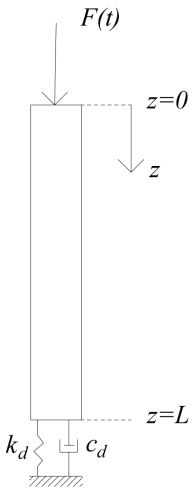

Figure 2-5: Boundary conditions for the rod model: a force at the top and a spring-dashpot system at the bottom.

2-5 Governing equations

Based on previous considerations, the equation of motion can be defined by the following equations:

$$c^2\frac{\partial^2 u}{\partial z^2} - \frac{\partial^2 u}{\partial t^2} + \frac{\nu^2 J}{A}\frac{\partial^2}{\partial t^2}\left(\frac{\partial^2 u}{\partial z^2}\right) = 0 \tag{2-13}$$

$$w(z,t) = -\nu R\frac{\partial u}{\partial z} \tag{2-17}$$

2-5-1 Boundary conditions

For the model of a one dimensional rod, there needs to be two boundary conditions to satisfy the equation of motion which includes a second derivative. Therefore the following two boundary conditions are assumed, as described by Figure 2-5:

1. the upper end of a rod is affected by an impact force which is time-dependent, leading to the condition in Eq. (2-25)

2. the bottom of the considered rod is constrained by a spring and a dash pot in z-direction at the lower end, roughly presenting the soil, which dissipates the energy in the pile. This assumption results in Eq. (2-26)

For this research, only the first downward travelling wave is relevant, and therefore a rough representation of the soil at the bottom is used. At this stage, the presence of a spring and dash-pot at the bottom of the pile does not have any influence on the shape of the first downward travelling wave and therefore it is not necessary to add a complex soil model as part of the simulation.

$$z = 0 \qquad c^2 \frac{\partial u}{\partial z}|_{z=0} + \frac{\nu^2 J}{A} \frac{\partial^2}{\partial t^2} \left(\frac{\partial u}{\partial z} \right) |_{z=0} = -\frac{F(t)}{\rho A} \tag{2-25}$$

$$z = L \qquad c^2 \frac{\partial u}{\partial z}|_{z=L} + \frac{\nu^2 J}{A} \frac{\partial^2}{\partial t^2} \left(\frac{\partial u}{\partial z} \right) |_{z=L} = -\frac{k_d}{\rho A} u|_{z=L} - \frac{c_d}{\rho A} \frac{\partial u}{\partial t}|_{z=L} \tag{2-26}$$

The boundary conditions are obtained by deriving equations of motions locally, using the Dirac-delta function. Integrating just around the location of the boundary condition results in a boundary condition without the Dirac-delta function. This derivation of boundary conditions is further elaborated in Appendix B.

2-5-2 Initial conditions

Besides the boundary conditions, the differential equation needs two initial conditions. At $t = 0$ both the longitudinal displacement and velocity of the pile are equal to zero, since the force has not hit the pile at this moment.

$$u(z, t = 0) = 0 \tag{2-27}$$

$$\dot{u}(z, t = 0) = 0 \tag{2-28}$$

2-5-3 Force

The shape of the applied force $F(t)$ is presented in Figure 2-6. A smooth impact force is applied using the theory developed by Deeks and Radolph [22]. This theory models the hammer impact analytically, based on a lumped ram and anvil masses. The ram and anvil are separated by a cushion, with internal damping. Furthermore, this system is connected to a pile, modelled as a dashpot.

2-6 Solution to governing equations in frequency domain

The last term of Eq. (2-13) includes derivations to both time and space. To find a solution to the equation of motion, two approaches can be adopted:

a) solving the system of equations in frequency domain

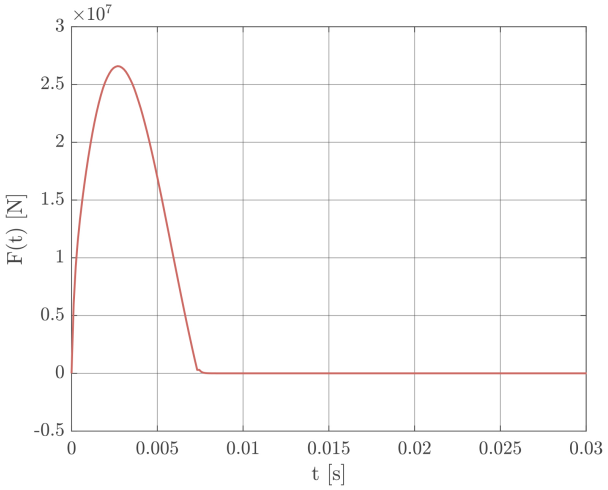

Figure 2-6: Input force $F(t)$

b) find a solution by using a numerical method in time domain

The first method gives a continuous solution in the frequency domain, which can be readily transformed into time domain. Additionally, the solution in the frequency domain offers further insight on the physics of the problem. The second method will solve the problem in time domain, but will have a numerical error and does not provide the physical information as the frequency method will do. Therefore, the first method is adopted.

In order to evaluate the solution in frequency domain, the equation of motion is transferred using the Fourier transform, with the following time-frequency relation:

$$f(t) = \frac{1}{2\pi}\int_{-\infty}^{\infty} \tilde{F}(\omega)e^{-i\omega t}d\omega \tag{2-29}$$

$$\tilde{F}(\omega) = \int_{-\infty}^{\infty} f(t)e^{i\omega t}dt \tag{2-30}$$

Applying this relation to our equation of motion results in:

$$\int_{-\infty}^{\infty}\left\{c^2\frac{\partial^2 u}{\partial z^2} - \frac{\partial^2 u}{\partial t^2} + \frac{\nu^2 J}{A}\frac{\partial^2}{\partial t^2}\left(\frac{\partial^2 u}{\partial z^2}\right) = 0\right\}e^{i\omega t}dt \tag{2-31}$$

$$c^2\frac{\partial^2 \tilde{u}}{\partial z^2} + \omega^2\tilde{u} - \omega^2\frac{\nu^2 J}{A}\frac{\partial^2 \tilde{u}}{\partial z^2} = 0 \tag{2-32}$$

$$\frac{\partial^2 \tilde{u}}{\partial z^2} + k_p^2\tilde{u} = 0 \tag{2-33}$$

$$\text{With} \quad k_p^2 = \frac{\omega^2}{c^2 - \omega^2\frac{\nu^2 J}{A}} \tag{2-34}$$

Where k_p is the wave number and $\tilde{u}$ denotes the complex-valued amplitude in the frequency domain. The wave number is the spatial frequency of a wave, in other words the number of waves (or cycles or radians) per unit distance.
The equation of motion is now a second order linear ordinary differential equation and a final solution for $\tilde{u}$ will therefore be of the form:

$$\tilde{u}(z,\omega) = C_1 \exp(ik_p(\omega)z) + C_2 \exp(-ik_p(\omega)z) \tag{2-35}$$

Transforming the boundary conditions from Eq. (2-25) and (2-26) into frequency domain gives:

$$\left(c^2 - \omega^2 \frac{\nu^2 J}{A}\right) \frac{\partial \tilde{u}}{\partial z}|_{z=0} = -\frac{\tilde{F}}{\rho A} \tag{2-36}$$

$$\left(c^2 - \omega^2 \frac{\nu^2 J}{A}\right) \frac{\partial \tilde{u}}{\partial z}|_{z=L} = -\frac{k_d}{\rho A}\tilde{u}|_{z=L} - i\omega \frac{c_d}{\rho A}\tilde{u}|_{z=L} \tag{2-37}$$

Constants C_1 and C_2 can be found by substituting Eq. (2-35) into the boundary conditions.

$$\left(c^2 - \omega^2 \frac{\nu^2 J}{A}\right) (ik_p C_1 - ik_p C_2) = -\frac{\tilde{F}}{\rho A} \tag{2-38}$$

$$\begin{aligned}\left(c^2 - \omega^2 \frac{\nu^2 J}{A}\right) (ik_p C_1 \exp(ik_p L) - ik_p C_2 \exp(-ik_p L)) = \\ - \left(\frac{k_d}{\rho A} + i\omega \frac{c_d}{\rho A}\right) (C_1 \exp(ik_p L) + C_2 \exp(-ik_p L))\end{aligned} \tag{2-39}$$

The following constants are then found:

$$C_1 = -\frac{\tilde{F} k_p}{\rho A i\omega^2 (1 - C_3)} \tag{2-40}$$

$$C_2 = C_1 \cdot C_3 \tag{2-41}$$

In which:

$$C3 = \exp(2ik_p L) \frac{i\omega^2 + k_p \frac{k_d}{\rho A} + i\omega k_p \frac{c_d}{\rho A}}{i\omega^2 - k_p \frac{k_d}{\rho A} - i\omega k_p \frac{c_d}{\rho A}} \tag{2-42}$$

Although an analytical solution is found it appears that Eq. (2-36) can be problematic when $c^2 = \omega^2 \frac{\nu^2 J}{A}$. This condition yields to a trivial solution in Eq. (2-33), stating that a $\tilde{u}$ has to be zero at this frequency. Therefore, the equation of motion only holds for frequencies below or above this critical frequency. This wavenumber issue will be further explained in the following section.

2-6-1 Wavenumber problem

As seen previously, the wavenumber can cause problems in the final analytical solution for $\tilde{u}$ when $c^2 = \omega^2 \frac{\nu^2 J}{A}$. This section will further elaborate on the wavenumber, which can be calculated as follows:

$$k_p^2 = \frac{\omega^2}{c^2 - \omega^2 \frac{\nu^2 J}{A}} \tag{2-34}$$

As seen in Eq. (2-34), k_p is positive and real when ω is relatively small, and it can be imaginary when ω becomes large. This phenomenon is also presented in Figure 2-7b. The critical radial frequency is found at:

$$\omega_c = \sqrt{\frac{c^2 A}{\nu^2 J}} \tag{2-43}$$

Hence, three cases can be distinguished:

1. $\omega < \omega_c$ - k_p is positive and real and results in propagating waves (travelling waves oscillating as a sinusoidal).
2. $\omega > \omega_c$ - k_p is imaginary and results in evanescent waves (waves exponentially decaying away from the edges of the pile at $z = 0$ or $z = L$).
3. $\omega = \omega_c$ (also $\omega \to \omega_c$) - k_p is infinite and according to Eq. (2-33), $\tilde{u}$ has to be zero.

In Figure 2-7 the influence of material damping is graphically presented. Material damping is included using $E = E(1 + 1i/500)$. This results in a peak at ω_c which is not infinite, in contrast with the plot of k_p without material damping. Also, the imaginary part of k_p in the plot with material damping, becomes negative.

Figure 2-8a presents k_p in complex plane. The red lines, representing the wavenumber k_p without damping are either real or imaginary, as stated before. Additionally, they go to infinity along all axes when the denominator of Eq. (2-34) reaches zero.

The green lines in Figure 2-8a represent k_p under material damping. Instead of being only real or imaginary, k_p is complex valued on all points. Furthermore, when the denominator of Eq. (2-34) goes to zero, the values of k_p are finite, in contrast to k_p without material damping. However, the values are still too large to obtain correct values for $u(z, t)$.

This singularity in Eq. (2-34) also gives insight into the pile's physics. As seen in Eq. (2-43) the diameter of a pile plays an important role in the critical frequency: increasing the diameter results in a lower critical frequency since $\omega_c \propto {}^1/_{D^2}$, as presented in Figure 2-8b. This means that for a larger diameter, the force pushing the pile down into the soil has to contain more energy in the lower frequencies. All the energy in the frequency range above the critical frequency produce evanescent waves. In other words, this energy is not efficiently used for pile driving.

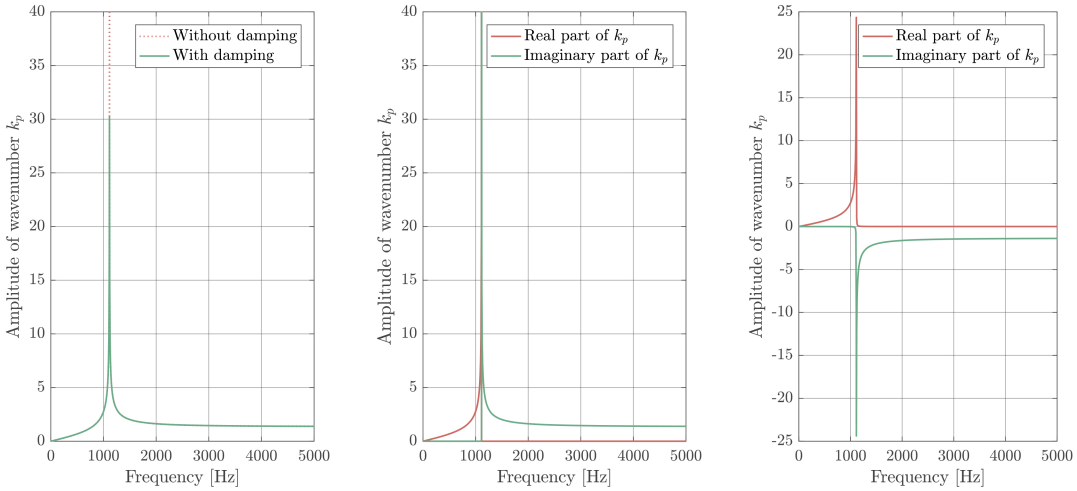

(a) Absolute value of k_p

(b) Real and imaginary value of k_p, without material damping

(c) Real and imaginary value of k_p, material damping included

Figure 2-7: Dispersion relation and influence of material damping

2-7 Frequency dependent damping

As discussed in the previous section, the analytical solution in the frequency domain presents a singularity. While that singularity is relevant to understand the physics of the problem, it also poses several numerical challenges. A frequency dependent damping is applied to reduce the influence of those frequencies which give numerical numerical problems, to achieve numerical stability.

In the previous section, a material damping $E = E(1 + i/500)$ was used. This leads to a small damping over the whole frequency spectrum. However, this damping does not correct the wavenumber values around the critical frequencies enough. In order to neglect the frequencies close to the critical frequency, but capture the rest of the spectrum, a frequency dependent damping is introduced: a high imaginary part is added for the frequencies required to be damped. The damping can therefore be seen as a filter, applied in frequency domain. This frequency damping is further explained in Section 2-7-1

2-7-1 Causality principle

Applying a frequency filter may lead to a non-causal signal in time domain. This means that the output of the filter depends on input of the future. In other words the pile "reacts", before the force acts on the pile.

Therefore, the filter (referred here as $\beta(t)$) has to be applied also in time domain, as a convolution integral:

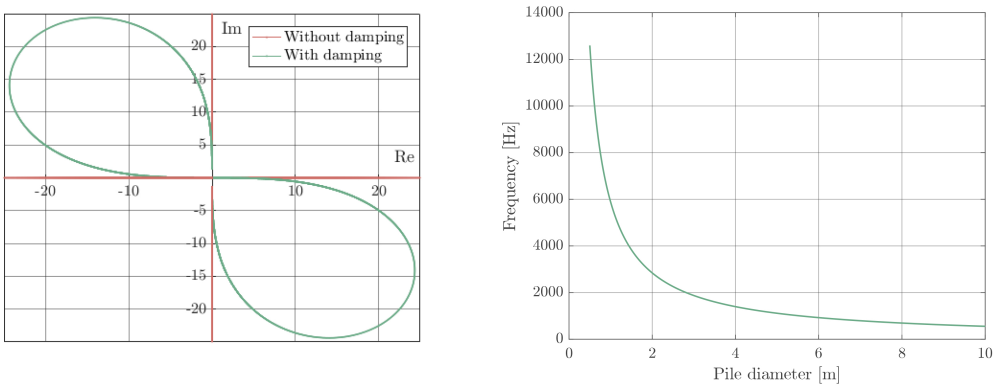

(a) **(b)**

Figure 2-8: Figure (a) presents k_p in complex plane, where the difference in use of damping is clearly presented. The wavenumber in which no damping is included is either real or imaginary and can go to infinity, while the wavenumber with damping can be complex valued and does not reach infinity. Figure (b) presents the relation between pile diameter and f_c and f_r , showing that an increase of pile diameter will decrease the value of the critical frequency and of the ring frequency. The ring frequency will always be smaller than the critical frequency.

$$c^2 \int_0^t \beta(t-\tau) \frac{\partial^2 u(z,\tau)}{\partial z^2} d\tau - \frac{\partial^2 u}{\partial t^2} + \frac{\nu^2 J}{A_p} \frac{\partial^2}{\partial t^2} \left(\frac{\partial^2 u}{\partial z^2} \right) = 0 \tag{2-44}$$

Transforming β into frequency domain gives the following:

$$\begin{aligned} \tilde{\beta}(\omega) &= \int_{-\infty}^{\infty} \beta(t) \exp(i\omega t) dt \\ &= \int_{-\infty}^{\infty} \beta(t) \cos(\omega t) dt + i \int_{-\infty}^{\infty} \beta(t) \sin(\omega t) dt \end{aligned} \tag{2-45}$$

Hence, $\tilde{\beta}(\omega)$ includes both an imaginary and a real part. The real part of damping $\tilde{\beta}(\omega)$ has to be equal to 1 or as close to 1 as possible, to take the correct (real) values for material constants in the equation of motion (Young's modulus and mass density) into account for those frequencies where damping is not needed. The imaginary part only should be high, at those values where damping is wanted. The following equation for β is introduced, a β which includes both of these requirements:

$$\beta(t) = A\delta(t) - B \exp(-\alpha t) \sin(\omega_c t) \tag{2-46}$$

$$\tilde{\beta}(\omega) = A - \frac{B\omega_c}{(i\omega + \alpha)^2 + \omega_c^2} \tag{2-47}$$

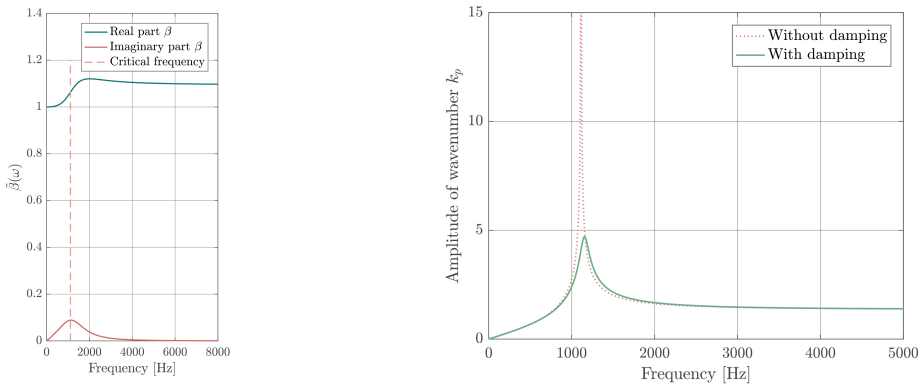

(a) **(b)**

Figure 2-9: Frequency dependent damping $\tilde{\beta}(\omega)$ in Young's Modulus presented in Figure (a) and its resulting wavenumber $k_p(\omega$ vs. undamped wavenumber in Figure (b).

Where ω_c presents the critical frequency discussed in Section 2-6-1. In these equations, A needs to be such that $Re(\tilde{\beta}(\omega)) = 1$, at least for the lower frequencies. Therefore:

$$A = 1 + (B\omega_c)/(\alpha^2 + \omega_c^2); \tag{2-48}$$

For each pile size, a B and α have to be found, such that the real part for the other frequencies are is also close to 1 and that the damping only affects the critical zone. An example of $\tilde{\beta}(\omega)$ and its corresponding wavenumber is presented in Figure 2-9.

2-8 Time domain

The previous sections presented a final solution for the longitudinal and radial deformation in frequency domain. Now, using the inverse Fourier transform (Eq. (2-30)), the results in time domain can be obtained. The pile's dimensions and material properties are described in Table 2-2.

Pile			
Length	L	30	m
Diameter	D	5	m
Wall thickness	h	70	mm
Young's Modulus	E	210	GPa
Mass density	ρ	7850	kg/m^3
Poisson's ratio	ν	0.3	

Table 2-2: Overview of pile dimensions and material properties

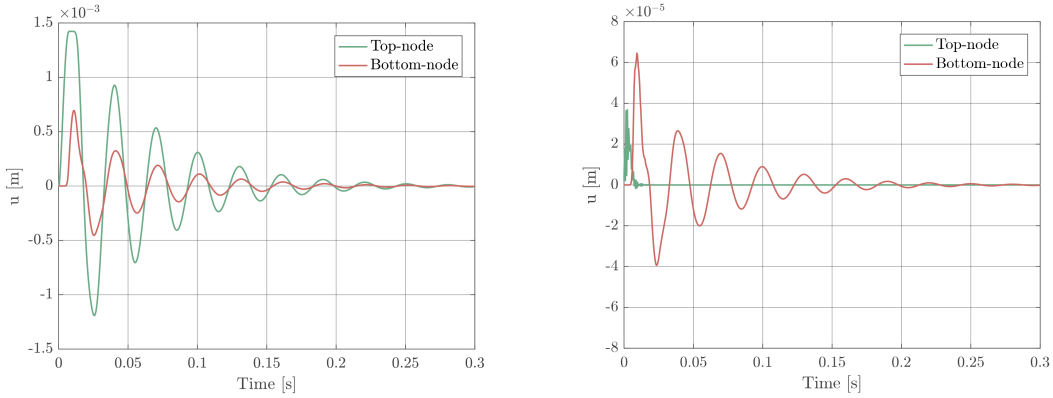

Figure 2-10: Longitudinal (a) and radial (b) displacement of a pile wall over time for the top and the bottom of a pile under influence of an impact load.

Figure 2-10 and Figure 2-11 present the first results from this part of the model. It is interesting to see that the bottom of the pile has a larger radial deformation over time than the top of the pile and the radial deformation at the top has a shorter period than its longitudinal deformation.

Looking at Figure 2-11, it can be seen that the longitudinal wave increases linear over time per node. The radial deformation is more inconsistent and here it shows why the duration of radial deformation at the top is shorter of time; pressing on the rod bulks out the middle part of the pile but the top is almost completely constrained. Since the bottom node is only constraint in z-direction, it here has the possibility to radiate outwards and therefore the duration and amplitude of radial deformation at the bottom are larger.

Besides this, it also can be seen that the slope of the radial propagating wave is larger at the start of the impact and due to the used material damping the slope decreases over time. This is important information for the purpose of this thesis; adjusting the pile's structure locally seems to be the most promising at the top of the pile. Decreasing the slope of the radial wave here, results in an even more decreased slope at the bottom of the pile, assuming that the slope of the radial wave starts the perturbation of the water and therefore also the noise pollution.

2-9 Conclusion

The purpose of this chapter was to define a method able to describe the longitudinal wave propagation in piles. A simple wave equation which includes lateral inertia effects, was chosen to be used for this analysis. This method provided a first approximation of the shape of a wave, travelling through a pile after impact loading. Besides this, the model gives a first insight in the shape of radial waves through a pile under impact

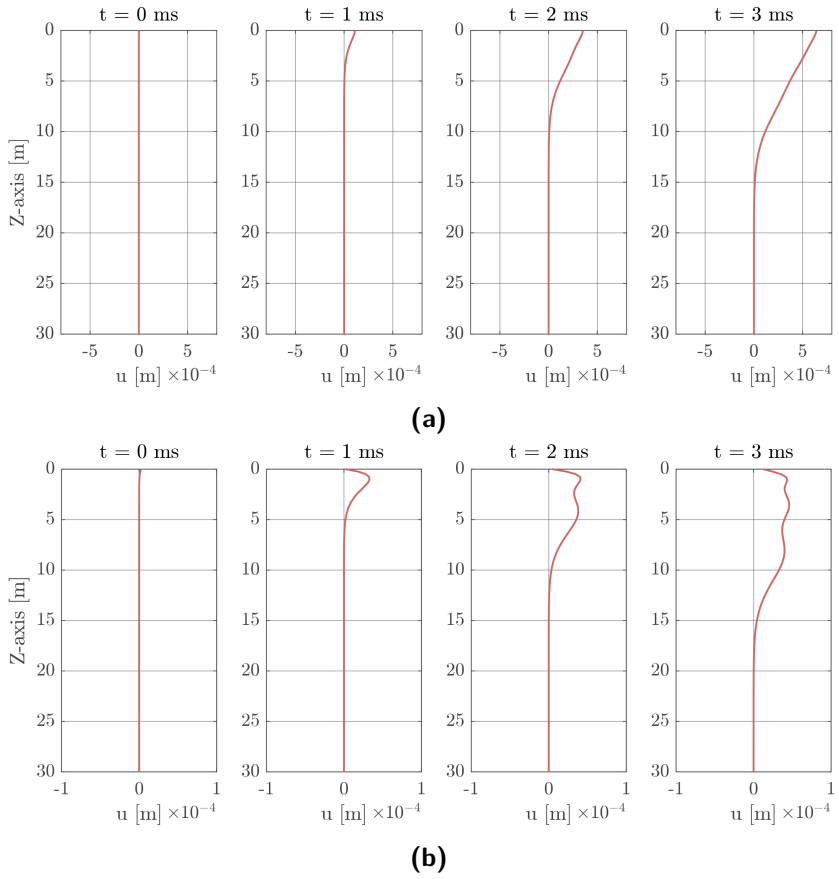

Figure 2-11: Longitudinal (a) and radial (b) displacement of a pile wall in time, under the influence of an impact load.

loading. It appears that the slope of the radial propagating wave is the steepest at the top and due to material damping the slope decreases. This is useful information for the purpose of this research: reducing underwater noise generation by (locally) adjusting the pile's dynamical structure.

Chapter 3

Acoustic perturbation of surrounding media

The previous chapter explained how monopiles are hammered into soil, a principle based on longitudinal waves. These waves form the base of the model to predict the origin of underwater noise and research how the waves in the pile affect the noise in the sea and how these waves can be adapted to reduce the noise emission. By perturbing the surrounding media, the longitudinal waves cause loud underwater noise, affecting marine life. In this chapter, this perturbation is further examined and the second part of the model is investigated: the acoustic medium.

3-1 Noise paths

During the installation phase, the monopile is surrounded by three media ([23],[24]): air, water and ground (the seabed), also presented in Figure 3-1. Pressure waves travel along each of these media-paths. However, not each path has an equal contribution to underwater noise.

The three different paths (see also Figure 3-1) are analysed and their individual contribution is described in [23] and [24]. A third [25] study quantifies these contributions to underwater noise.

The airborne path does not contribute significantly to the underwater noise pollution. Due to a large impedance gap between air and water, acoustic waves travelling through air will mostly be reflected at the interface between water and air.
The waterborne path, however, has a low impedance, because the density of water has the same order of magnitude the density of steel. Additionally, high sound speed in water and in steel lead to impact-induced waves that transform into waves travelling

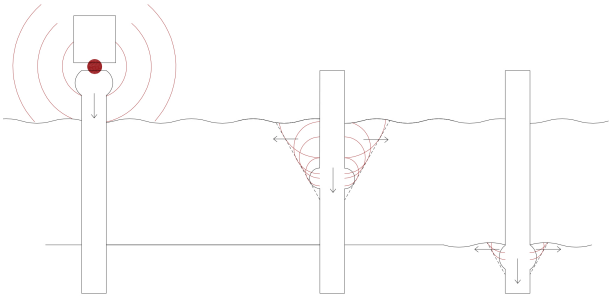

Figure 3-1: Noise paths in surrounding media due to travelling waves in a monopile. From the left to the right: the noise path in air, the path through water and the path through the soil.

through water. Due to these characteristics, the waterborne path is usually considered as the primary noise path.
At the end of a pile, the force is exerted onto the soil. The structural waves travel further into the ground as elastic waves (waves that include both compressional and shear motion of soil particles). These elastic waves radiate outwards and may therefore also 'leak' back into the water column where they contribute to underwater noise from the waterborne wave, as a secondary noise path. The soil has a high damping factor comparing to water; high frequencies will therefore be mostly damped out in the soil and almost only low frequency waves travel through the soil.

The waterborne path is the largest contributor to the underwater noise reaching mammals. However, the relative contribution of each part will depend on the specific conditions of the whole system. Mitigation solutions focussing on the waterborne path are able to significantly reduce the radiating noise due to the contribution of this path, but its effectiveness can be limited in some cases by the groundborne path, in which the noise distrubance can travel longer distances from the source [25][14]. It is also worth noticing that the current trend suggests the monopiles will become heavier and larger in the future. These piles will have lower eigenfrequencies, making the groundborne path a larger contributor to the underwater noise porblem, and reducing further the effectiveness of current mitigation systems described in Chapter 1.

3-2 Pressure waves in fluids

Waves in water in terms of pressure can be described as in Eq. (3-1), assuming an ideal incompressible fluid ([26],[27]).

$$\frac{\partial^2 p}{\partial t^2} = c_w^2 \nabla^2 p \tag{3-1}$$

Figure 3-2: Frame of the 2D model, including the boundary conditions

with c_w as the speed of sound in the seawater (approximately 1500 [m/s]) and ∇^2 as the Laplacian described in the cylindrical coordinate system.
Expanding, Eq. (3-1) leads to:

$$\begin{aligned}\frac{\partial^2 p}{\partial t^2} &= c_w^2 \left(\frac{1}{r} \frac{\partial}{\partial r} \left(r \frac{\partial p}{\partial r} \right) + \frac{\partial^2 p}{\partial z^2} \right) \\ &= c_w^2 \left(\frac{\partial^2 p}{\partial r^2} + \frac{1}{r} \frac{\partial p}{\partial r} + \frac{\partial^2 p}{\partial z^2} \right)\end{aligned} \tag{3-2}$$

Since the water is considered incompressible here (i.e. ρ is constant), the wave equation can be simplified by using the scalar velocity potential: $\mathbf{v} = \nabla\phi$ [26][27]. This equation describes the scalar velocity potential, φ. Due to the relations between $\mathbf{v}$ and p, as presented in Eq. (3-4) and (3-5), the acoustic wave equation can facilitate coupling with different structure systems, an advantage comparing to the pressure wave equation Eq. (3-2).

$$\frac{\partial^2 \varphi}{\partial t^2} = c_w^2 \left(\frac{\partial^2 \varphi}{\partial r^2} + \frac{1}{r} \frac{\partial \varphi}{\partial r} + \frac{\partial^2 \varphi}{\partial z^2} \right) \tag{3-3}$$

With relations:

$$p = -\rho \frac{\partial \varphi}{\partial t} \tag{3-4}$$

$$\mathbf{v} = \nabla \varphi \tag{3-5}$$

3-2-1 Boundary conditions

For the model of the acoustic medium a 3D model, which is treated as cylindrically symmetric configuration, as presented in Figure 3-2. On the left side of the figure the water is bounded by a monopile which is affected by an impact load. The speed of

the radial deformation of a monopile as a result of downward travelling waves, is the same as the speed of water particles at the monopile-water interface. Therefore the first boundary condition is of the kinematic type and is given in Eq. (3-6). On the right hand, the sea extends to $r \to \infty$, from which the pressure waves propagating outwards does not return. This boundary condition is described by Eq. (3-7) as the radiation condition [26], [1]. At the top side, the acoustic medium is limited by the interface between the water and the air. At this interface there will be a pressure release boundary, and the variations in pressure will be zero as in Eq. (3-8). At the bottom the interface between the water and the sea bed is assumed to be acoustically rigid, which means that the vertical velocity of the fluid is zero, as described in Eq. (3-9).

$$r = r_0; \qquad v_r = \dot{w}(z,t) \to \frac{\partial \varphi}{\partial r} = \dot{w}(z,t) \tag{3-6}$$

$$r = \infty; \qquad \lim_{r\to\infty} r\left(\frac{\partial \varphi}{\partial r} + k\varphi\right) = 0 \tag{3-7}$$

$$z = 0: \qquad p = 0 \to -\rho\frac{\partial \varphi}{\partial t} = 0 \tag{3-8}$$

$$z = L: \qquad v_z = 0 \to \frac{\partial \varphi}{\partial z} = 0 \tag{3-9}$$

In equation Eq. (3-7), k equals the angular wavenumber $k^2 = \frac{\omega^2}{c^2}$.
As can be seen, there are boundary conditions concerning water pressure and boundary conditions concerning the particle velocity. The boundary conditions concerning the particle velocity cannot easily be implemented using the pressure wave equation Eq. (3-2). As an alternative, the equations are solved using the acoustic wave equation (Eq. (3-3)).

3-3 Solution

The equations can be solved in frequency domain, by using the Fourier transformation as described in Eq. (2-29) and (2-30).

This transformation results in the Helmholtz equation:

$$\int_{-\infty}^{\infty} \left\{ c^2 \left(\frac{\partial^2 \varphi}{\partial r^2} + \frac{1}{r}\frac{\partial \varphi}{\partial r} + \frac{\partial^2 \varphi}{\partial z^2} \right) - \frac{\partial^2 \varphi}{\partial t^2} = 0 \right\} e^{i\omega t} dt \to \tag{3-10}$$

$$\to \quad \nabla^2 \tilde{\varphi}(r,z,\omega) + k^2 \tilde{\varphi}(r,z,\omega) = 0 \tag{3-11}$$

where $k^2 = \frac{\omega^2}{c^2}$, as the angular wavenumber, and $\tilde{\varphi}$ is the Fourier transform of ϕ.

The boundary conditions can be rewritten in the frequency domain too:

$$r = r_0; \qquad \frac{\partial \tilde{\varphi}}{\partial r} = i\omega \tilde{w}(z,t) \tag{3-12}$$

$$r = \infty; \qquad \lim_{r\to\infty} r\left(\frac{\partial \tilde{\varphi}}{\partial r} + ik\tilde{\varphi}\right) = 0 \tag{3-13}$$

$$z = 0: \qquad -i\omega\rho\tilde{\varphi} = 0 \tag{3-14}$$

$$z = L: \qquad \frac{\partial \tilde{\varphi}}{\partial z} = 0 \tag{3-15}$$

The equation of motion Eq. (3-11) can be solved for $\tilde{\varphi}(r,z,\omega)$ using the separation of variables method:

$$\tilde{\varphi}(r,z,\omega) = F(r)\cdot S(z) \tag{3-16}$$

Substituting this into the Helmholtz equation, gives Eq. (3-17).

$$S\frac{d^2F}{dr^2} + S\frac{1}{r}\frac{dF}{dr} + F\frac{d^2S}{dz^2} + k^2FS = 0 \tag{3-17}$$

$$S\frac{d^2F}{dr^2} + S\frac{1}{r}\frac{dF}{dr} = -F\frac{d^2S}{dz^2} - k^2FS \tag{3-18}$$

$$\frac{1}{F}\frac{d^2F}{dr^2} + \frac{1}{F}\frac{1}{r}\frac{dF}{dr} = -\frac{1}{S}\frac{d^2S}{dz^2} - k^2 \tag{3-19}$$

The left hand side and the right hand side of Eq. (3-19) depend on a different variable. Therefore, Eq. (3-19) can only be true if both sides are constant. This unknown constant is called k_r^2, which later on appears to be the radial wavenumber. Then, this equation can be separated in two equations (Eq. (3-20) and (3-21)):

$$\frac{d^2S}{dz^2} + (k^2 - k_r^2)S = 0 \tag{3-20}$$

$$\frac{d^2F}{dr^2} + \frac{1}{r}\frac{dF}{dr} + k_r^2F = 0 \tag{3-21}$$

In these equations k^2 is $\frac{\omega^2}{c^2}$, the angular wavenumber, and k_r^2 is the unknown separation constant (the radial wavenumber). Eq. (3-20) is known as the normal mode equation or depth equation [28], describing the standing wave portion of the solution. Eq. (3-21) is the zero order Bessel equation, describing the wave in the horizontal direction. Together these two functions describe each normal mode as a travelling wave in the horizontal direction and a standing wave in the vertical direction.

Assuming the vertical wavenumber is $k_z^2 = k^2 - k_r^2$, the solution to the depth equation (Eq. (3-20)) is of the form of Eq. (3-22).

$$S(z) = C_1 \sin(k_z z) + C_2 \cos(k_z z) \tag{3-22}$$

Using the boundary conditions in z-direction (Eq. (3-14) and (3-15)), the final solution of Eq. (3-27) can be found.

$$z = 0 \quad -i\omega\rho S(z) = 0 \tag{3-23}$$

$$-i\omega\rho C_2 = 0 \rightarrow C_2 = 0 \tag{3-24}$$

$$z = z_2 \quad \frac{dS}{dz} = 0 \tag{3-25}$$

$$k_z C_1 \cos(k_z z_2) = 0 \rightarrow k_{z,n} = \frac{(2n+1)\pi}{2(z_2 - z_1)} \text{ and } n = 0, 1, 2...\infty \tag{3-26}$$

$$\rightarrow \quad S(z) = \sum_{n=0}^{\infty} C_n \sin(k_{z,n}(z - z_1)) \tag{3-27}$$

$$\text{With } \; k_{z,n} = \frac{(2n+1)\pi}{2(z_2 - z_1)} \text{ and } n = 0, 1, 2...\infty \tag{3-28}$$

Next step is to solve Eq. (3-21), which is a Bessel equation of zeroth order [29]. In general a Bessel equation of order n^{th} can be solved by using the Hankel functions of the first ($H_n^{(1)}$) and second kind ($H_n^{(2)}$). Given these two facts, a solution for Eq. (3-21) can be found in the form of:

$$F(r) = \sum_{n=0}^{\infty} C_{3n} H_0^{(1)}(k_{r,n} r) + C_{4n} H_0^{(2)}(k_{r,n} r) \tag{3-29}$$

For the chosen time-frequency transform as discussed previously, the first Hankel function represents the outgoing waves while the second Hankel function represents the incoming waves. For a cylinder (monopile) in a free space, as in this thesis, the ingoing waves should be neglected and only the outgoing wave exists, as the radiation condition in Eq. (3-13) stated [30]. This means that $C_4 = 0$ and therefore:

$$F(r) = \sum_{n=0}^{\infty} C_n H_0^{(1)}(k_{r,n} r) \tag{3-30}$$

The longitudinal mode wavenumbers $k_{z,n}$ are always real and positive. With $k_{r,n}^2 = \sqrt{k^2 - k_{z,n}^2}$, this means that two cases exist:

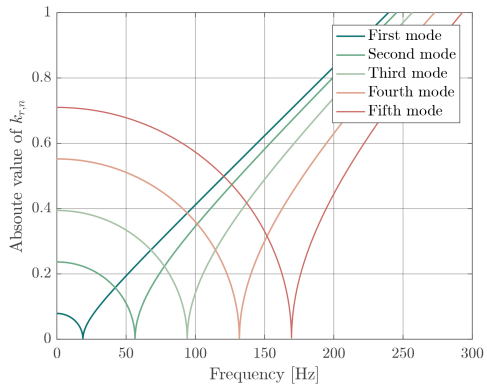

Figure 3-3: Radial wavenumber against frequency . This figure shows that $k_{r,n}$ will be zero in each mode at one frequency. This happens when when $k = k_{z,n}$, which holds for one frequency per mode number.

1. $k^2 - k_{z,n}^2 > 0$ - Wavenumber $k_{r,n}$ is real and either positive or negative due to the sign of its roots. These radial wavenumbers represent propagating pressure waves.

2. $k^2 - k_{z,n}^2 < 0$ - Wavenumber $k_{r,n}$ is imaginary and either positive or negative due to the sign of its roots. These radial wavenumbers represent evanescent pressure waves.

There exists a finite number of propagating modes and an infinite number of evanescent waves per frequency. The frequency for which no propagating mode exists is called the cut-off frequency. This means that if the frequency is below this cut-off frequency, even the first mode does not have real wavenumbers. Below this frequency no energy can propagate through the fluid. The cut-off frequency is calculated as follows:

$$\frac{\omega_0^2}{c^2} = k_{z,0}^2 \tag{3-31}$$

$$\frac{\omega_0^2}{c^2} = \left(\frac{2 \cdot 0 + 1}{2(z_2 - z_1)}\pi\right)^2 \tag{3-32}$$

$$\omega_0 = \frac{c\pi}{2(z_2 - z_1)} \quad [\text{rad/s}] \tag{3-33}$$

$$f_0 = \frac{c}{4(z_2 - z_1)} \quad [\text{Hz}] \tag{3-34}$$

For those cases where $k = k_{z,n}$ (one frequency per mode, see Figure 3-3), the radial wavenumber $k_{r,n}$ is zero. For these cases $H_0^{(1)}(k_{r,n}r) \to \infty$. In the model, the frequency has a discrete character and the 'problematic' frequencies are approximated by frequencies close to them, but the frequency itself is not used to provide numerical stability.

Both functions $S(z)$ and $F(r)$ are now proposed (in Eq. (3-27) and (3-30) respectively) and the total solution of $\tilde{\varphi}$ is therefore equal to:

$$\tilde{\varphi}(r,z,\omega) = \sum_{n=0}^{\infty} C_n H_0^{(1)}(k_{r,n} r) \sin(k_{z,n}(z - z_1)) \tag{3-35}$$

For each mode $\tilde{\phi}(r,z,\omega)$ still contains one unknown C_n. This can be solved with the remaining boundary condition from Eq. (3-12). The particle velocity equation along the r-coordinate reads:

$$\tilde{v}_r(r,z,\omega) = \frac{\partial \tilde{\varphi}}{\partial r} \tag{3-36}$$

$$= \frac{\partial}{\partial r}\left(\sum_{n=0}^{\infty} C_n H_0^{(1)}(k_{r,n} r) \sin(k_{z,n}(z - z_1)))\right) \tag{3-37}$$

$$= -\sum_{n=0}^{\infty} C_n k_{r,n} H_1^{(1)}(k_{r,n} r) \sin(k_{z,n}(z - z_1)) \tag{3-38}$$

where

$$\frac{\partial}{\partial r}\left(H_0^{(1)}(k_{r,n} r)\right) = -k_{r,n} H_1^{(1)}(k_{r,n} r) \tag{3-39}$$

At $r = r_0$, Eq. (3-6) (Eq. (3-12) in frequency domain) needs to be satisfied at all times:

$$\tilde{v}_r(r,z,\omega) = i\omega\left[\tilde{w}(z,\omega)\right] \tag{3-40}$$

From Eq. (3-38) = Eq. (3-40) and using the orthogonality principle of the fluid modes in the domain $z = z_1$ and $z = z_2$, constant C_n can be found:

$$\int_{z_1}^{z_2} \left[-\sum_{n=0}^{\infty} C_n k_{r,n} H_1^{(1)}(k_{r,n} r_0) \sin(k_{z,n}(z - z_1)) = i\omega\left[\tilde{w}(z,\omega)\right]\right] \sin\left(k_{z,m}(z - z_1)\right) dz \tag{3-41}$$

Eq. (3-41) results in:

$$C_n = \frac{-2i\omega}{(z_2 - z_1) k_{r,n} H_1^{(1)}(k_{r,n} r_0)} \int_{z_1}^{z_2} \tilde{w}(z,\omega) \sin\left(k_{z,n}(z - z_1)\right) dz \tag{3-42}$$

Given Eq. (3-35) and Eq. (3-42), $\tilde{\varphi}$ is known; from the Fourier transform of Eq. (3-4) the pressure in frequency domain is:

$$\tilde{p}(r,z,\omega) = -i\omega\rho\tilde{\varphi}(r,z,\omega) \tag{3-43}$$

$$= -\frac{2\omega^2\rho}{(z_2-z_1)}\sum_{n=0}^{\infty} Q_n(r,z,\omega)\int_{z_1}^{z_2}\tilde{w}(z,\omega)\sin\left(k_{z,n}(z-z_1)\right)dz \tag{3-44}$$

In which:

$$Q_n(r,z,\omega) = \frac{H_0^{(1)}(k_{r,n}r)}{k_{r,n}H_1^{(1)}(k_{r,n}r_0)}\sin(k_{z,n}(z-z_1)) \tag{3-45a}$$

$$k^2 = \frac{\omega^2}{c^2} \tag{3-45b}$$

$$k_{z,n} = \frac{(2n+1)\pi}{2(z_2-z_1)} \text{ and } n = 0,1,2...\infty \tag{3-45c}$$

$$k_{r,n} = \sqrt{k^2 - k_{z,n}^2} \tag{3-45d}$$

3-4 Truncation criteria

As stated before, there will be a finite number of propagating fluid modes at each frequency and an infinite number of evanescent fluid modes. Therefore, the infinite series in Eq. (3-43) needs to be truncated to describe an upper limit for summation index n of the fluid modes. The error created with this truncation should not be too high and thus some criteria are needed.

All propagating modes will be included in the model. The higher the frequency, the higher the number of propagating modes, as can be seen in Eq. (3-45d).

Regarding the evanescent modes: the solution will include as many modes as necessary to achieve a truncation error smaller than 1%. The truncation error can be measured against different criteria. In particular, Tsouvalas [31] investigated two convergence criteria to evaluate the contribution of the evanescent modes:

1. Convergence criterion based on a displacement mismatch at the pile-fluid interface; this criterion is based on the displacement of the fluid particles, along to the pile wall, which have to be equal to the pile wall's displacement.
2. Convergence criterion based on the error of propagating modes in the fluid; the criterion is based on the energy radiation into the fluid, for which a correct number of propagating modes have to be included (the acoustic energy is only dependent on propagating waves, since the evanescent modes do not carry any energy).

The first criterion gives a larger error than the truncation error on propagating modes and additionally provides better accuracy for the prediction of forces and bending moments in a pile. Therefore, the displacement criterion will be used for the purpose of this research.

Pile					Water			
Length	L	30	m		Surface level	z_1	10	m
Diameter	D	5	m		Seabed level	z_2	30	m
Wall thickness	h	70	mm		Mass density	ρ_w	1025	kg/m^3
Young's Modulus	E	210	GPa					
Mass density	ρ	7850	kg/m^3					
Poisson's ratio	ν	0.3						

Table 3-1: Overview of the pile's dimensions, material properties and properties of the fluid domain in the model

The displacement mismatch can be calculated as follows:

$$\partial u(z) = \left| \frac{\tilde{w}(z,\omega) - \tilde{u}_r(r = r_0, z, \omega)}{\tilde{w}(z,\omega)} \right| \tag{3-46}$$

Where $\tilde{u}_r$ is the fluid displacement:

$$\tilde{u}_r(r_0, z, \omega) = \frac{2}{z_2 - z_1} \sum_{n=0}^{\infty} \sin(k_{z,n}(z - z_1)) \int_{z_1}^{z_2} \tilde{w}(z,\omega) \sin(k_{z,n}(z - z_1)) dz \tag{3-47}$$

Figure 3-4 presents the result of the different number of evanescent modes included in the fluid model. For this case, with the system's parameters as described in Table 3-1, it appears that 80 evanescent modes, in addition to the finite number of propagating modes, are enough to meet the requirements as stated before.

3-5 Results

Figure 3-5 presents the pressures in the water in frequency domain, measured at different distances from the pile and all 5 m above seabed. In this figure, one can see the influence of the cut-off frequency; up to this frequency the amplitudes of the pressure are relatively small and only after this frequency the energy of the pressure starts to increase. Also the water damping is visible in the graph; the amplitudes of the pressure are significantly smaller for the locations far away from the pile compared to the pressures of the locations close by.

In order to analyse the water pressure with respect to time, Eq. (3-43) has to be numerically transformed back to the time domain with the inverse Fourier transform as found in Eq. (2-30). Figure 3-6a shows the pressures in time domain, at the same locations as in the previous figure. Also here the influence of water damping is visible in the amplitudes of the pressure at different locations, which also can be seen in Figure 3-6b. Additionally, one can see that it takes a few milliseconds for the pressure waves to affect the locations further away from the pile, hence the model gives causal results.

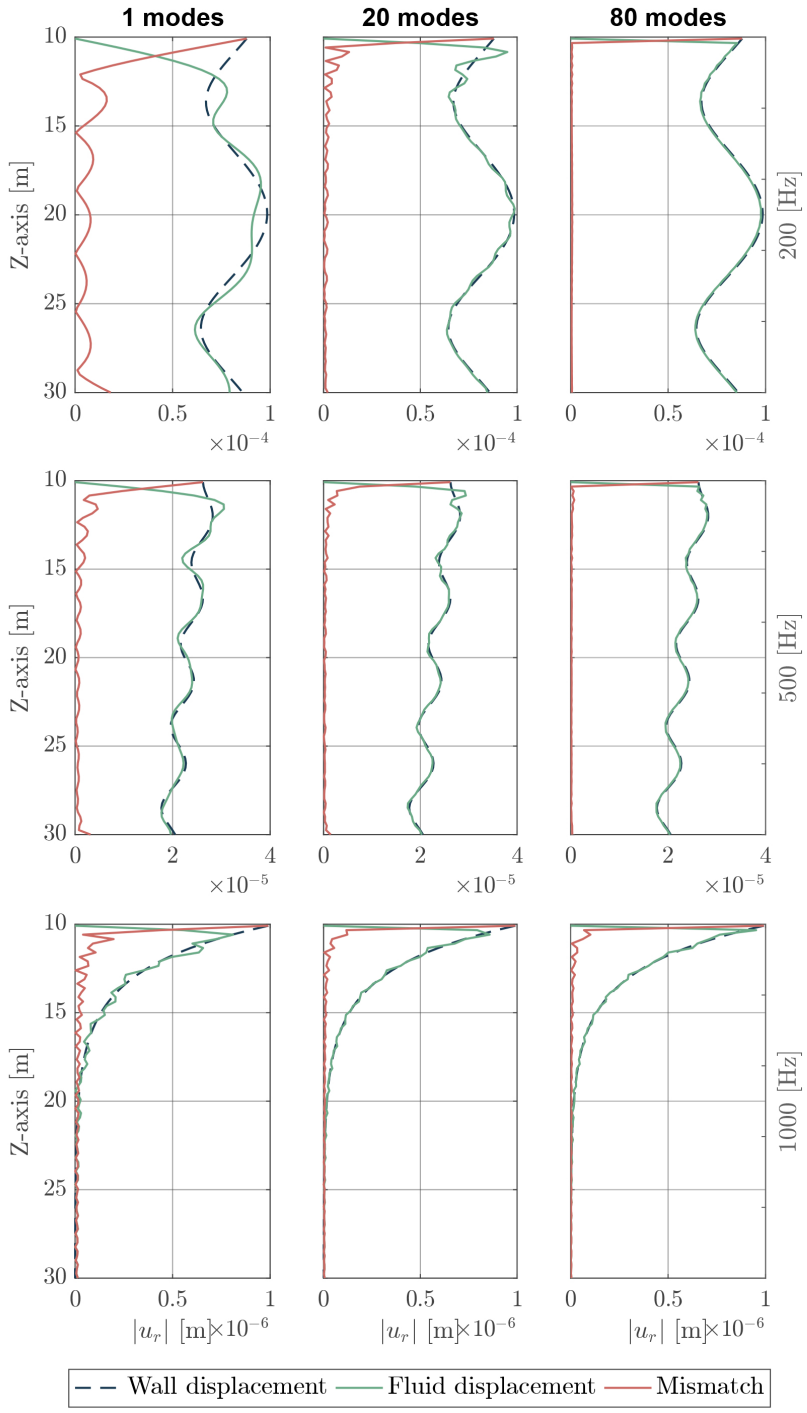

Figure 3-4: Radial displacement mismatch in fluid. The topfigures present the mismatch at 200 Hz, the middle presents the mismatch at 500 Hz and the bottom figures at 1000 Hz. From the left to the right column are respectively 1 evanescent mode, 20 and 80 evanescent modes included . As seen, the fluid displacement becomes more accurate when an increasing number of evanescent modes is included.

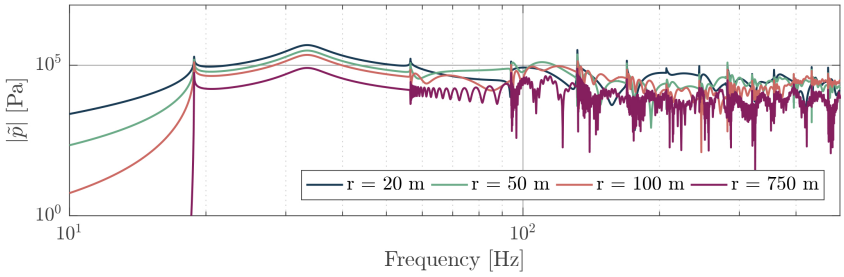

Figure 3-5: Pressures in frequency domain at different distances from the pile and measured 5 m above the seabed.

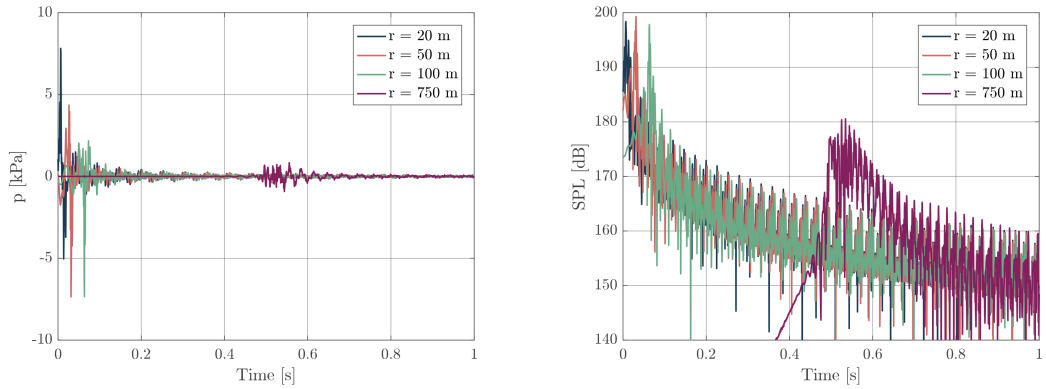

Figure 3-6: Figure (a) presents the pressure of the fluid at different distances from the pile, measured at 5 m above seabed. Figure (b) presents the Sound Pressure Levels for the same locations

3-6 Conclusion

In this chapter a model is proposed to analyse pressure waves in an acoustic medium like water. The model is based on the acoustic wave equation and a solution is found by the separation of variables method in the frequency domain. In combination with the model of the previous chapter, which described longitudinal waves through a pile due to an impact load, the acoustic model showed the evolution of pressure waves caused by these longitudinal waves. From the first results, one can conclude that the cut-off frequency has a significant influence on the results: below this frequency there is no energy exchange from the pile into the water.

Chapter 4

Coupling of deformation and acoustic medium

Chapter 2 described a model for simulating longitudinal and radial waves through a pile. In Chapter 3, this model is expanded by adding an acoustic medium.
For the last two chapters, it has been assumed that the water pressure does not have any influence on the longitudinal deformation (and on the radial deformation) of a pile under impact loading. However, in reality the pressure of the water does change the dynamics of the pile. In other words, the higher external pressures on the pile, the more the pile will be obstructed to radiate outwards, which leads to smaller longitudinal deformations. To find out what the actual influence of pressure is on the pile's deformation in this model, this chapter introduces a method to couple the deformation with the pressure in the acoustic medium.

4-1 Governing equations

Previously, it was assumed that the following equations held for the radial deformation and for the pressure in an acoustic medium, both in frequency domain:

$$\tilde{u}(z,\omega) = C1\exp(ik_p(\omega)z) + C2\exp(-ik_p(\omega)z) \tag{4-1}$$

$$\tilde{w}(z,t) = -\nu R\frac{\partial \tilde{u}}{\partial z} \tag{4-2}$$

$$\tilde{p}(r,z,\omega) = -\frac{2\omega^2\rho_w}{(z_2-z_1)}\sum_{n=0}^{\infty} Q_n(r,z,\omega)\int_{z_1}^{z_2}\tilde{w}(z,\omega)\sin\left(k_{z,n}(z-z_1)\right)dz \tag{4-3}$$

In which:

$$C_1 = -\frac{\tilde{F}k_p}{\rho A i\omega^2(1-C_3)} \tag{4-4a}$$

$$C_2 = C_1 \cdot C_3 \tag{4-4b}$$

$$C_3 = \exp(2ik_pL)\frac{i\omega^2 + k_p\frac{k_d}{\rho A} + i\omega k_p\frac{c_d}{\rho A}}{i\omega^2 - k_p\frac{k_d}{\rho A} - i\omega k_p\frac{c_d}{\rho A}} \tag{4-4c}$$

$$Q_n(r,z,\omega) = \frac{H_0^{(1)}(k_{r,n}r)}{k_{r,n}H_1^{(1)}(k_{r,n}r_0)}\sin(k_{z,n}(z-z_1)) \tag{4-4d}$$

$$k^2 = \frac{\omega^2}{c^2} \tag{4-4e}$$

$$k_{z,n} = \frac{(2n+1)\pi}{2(z_2-z_1)} \text{ and } n = 0,1,2...\infty \tag{4-4f}$$

$$k_{r,n} = \sqrt{k^2 - k_{z,n}^2} \tag{4-4g}$$

$$k_p = \sqrt{\frac{\omega^2}{c^2\tilde{\beta}(\omega) - \omega^2\frac{\nu^2 J}{A}}} \tag{4-4h}$$

The pressure in the acoustic medium already depends on the radial deformation of the pile. The longitudinal deformation, however, needs to be adjusted in order to include the pressure of the acoustic medium into the equation of motion. Therefore, a new equation of motion is derived using the energy method, the same way as done previously by Love [19] and Graff [20]. The full elaboration of this derivation can be found in Appendix C. Eq. (4-5) presents this new equation of motion.

$$c^2\beta(t)\frac{\partial^2 u}{\partial z^2} - \frac{\partial^2 u}{\partial t^2} + \frac{\nu^2 J}{A}\frac{\partial^2}{\partial t^2}\left(\frac{\partial^2 u}{\partial z^2}\right) - \frac{\nu}{\rho}p(r_0,z,t) = 0 \tag{4-5}$$

Transforming this into frequency domain results in the following:

$$c^2\tilde{\beta}(\omega)\frac{\partial^2\tilde{u}}{\partial z^2} + \omega^2\tilde{u} - \omega^2\frac{\nu^2 J}{A}\frac{\partial^2\tilde{u}}{\partial z^2} - \frac{\nu}{\rho}\tilde{p}(r_0,z,\omega) = 0 \tag{4-6}$$

$$\frac{\partial^2\tilde{u}}{\partial z^2} + k_p^2\tilde{u} - \frac{1}{c^2\tilde{\beta}(\omega) - \omega^2\frac{\nu^2 J}{A}}\frac{\nu}{\rho}\tilde{p}(r_0,z,\omega) = 0 \tag{4-7}$$

4-2 Solution to governing equations

The system of equations in frequency domain (Eq. (4-3) and (4-7)) can be rewritten by describing $\tilde{w}$ as a function of $\tilde{u}$. This makes it possible to solve the equation of motion

Eq. (4-7) including a pressure term in terms of $\tilde{u}$ instead of $\tilde{p}$.

$$\tilde{p}(r,z,\omega) = -\frac{2\omega^2\rho_w}{(z_2-z_1)}\sum_{n=0}^{\infty} Q_n(r,z,\omega)\int_{z_1}^{z_2} -\nu R\frac{\partial\tilde{u}}{\partial z}\sin\left(k_{z,n}(z-z_1)\right)dz \tag{4-8}$$

$$= \nu R\frac{2\omega^2\rho_w}{(z_2-z_1)}\sum_{n=0}^{\infty} Q_n(r,z,\omega)\int_{z_1}^{z_2} \frac{\partial\tilde{u}}{\partial z}\sin\left(k_{z,n}(z-z_1)\right)dz \tag{4-9}$$

Due to the integration term in the equation of motion for $\tilde{u}$ it is not possible to find an analytical solution. It is, however, possible to find a semi-analytical solution using the modal expansion technique.

This technique assumes that $\tilde{u}(z,\omega)$ is a superposition of normal modes of free vibrations, multiplied by an unknown function of frequency:

$$\tilde{u}(z,\omega) = \sum_{q=0}^{\infty} A_q(\omega)U_q(z) \tag{4-10}$$

In this equation, A_q is the amplitude factor per mode and $U_q(z)$ are the eigenmodes. First, the shape of each eigenmode needs to be defined, by substituting Eq. (4-10) into Eq. (4-7). The eigenmodes can then be used to calculate each amplitude factor.

4-2-1 Eigenmodes

Since the eigenmodes U_q only depend on z, they are not able to meet boundary conditions which depend on frequency. Therefore the equation of motion not only has to include the fluid pressure, but also the frequency dependent terms from the original boundary conditions (applied hammer force and bottom dashpot).

$$\frac{\partial^2\tilde{u}}{\partial z^2} + k_p^2\tilde{u} = B\left(\frac{\nu}{\rho}\tilde{p}(r_0,z,\omega) - \frac{\tilde{F}(\omega)}{\rho A}\delta(z) + i\omega\frac{c_d}{\rho A}\tilde{u}\ \delta(z-L)\right) \tag{4-11}$$

With

$$B = \frac{1}{c^2\tilde{\beta}(\omega) - \omega^2\frac{\nu^2 J}{A}} \tag{4-12}$$

In Eq. (4-10) $U_q(z)$ is the only function dependent of z and therefore has to meet the boundary conditions and the equation of motion for free vibrations. The equation of motion for free vibrations in modal domain is as follows:

$$\frac{\partial^2 U_q}{\partial z^2} + \gamma_q^2 U_q = 0 \tag{4-13}$$

With:

$$\gamma_q = \sqrt{\frac{\Omega_q^2}{c^2 - \Omega_q^2 \frac{\nu^2 J}{A}}} \tag{4-14}$$

In which Ω_q are the eigenfrequencies belonging to each eigenmode.

Now that the previous boundary conditions have partly moved into the equation of motion, the rod will be free at the top and only constrained by a spring at the bottom and the following boundary conditions hold:

$$z = 0 \qquad \frac{\partial U_q}{\partial z} = 0 \tag{4-15}$$

$$z = L \qquad \left(c^2 - \Omega_q^2 \frac{\nu^2 J}{A}\right) \frac{\partial U_q}{\partial z} = -\frac{k_d}{\rho A} U_q \tag{4-16}$$

Based on the above equations, a function for $U_q(z)$ can be found in the form of:

$$U_q(z) = C_1 \cos(\gamma_q z) + C_2 \sin(\gamma_q z) \tag{4-17}$$

Following from Eq. (4-15), $C_2 = 0$. Then implementing Eq. (4-16) gives:

$$\begin{gathered} -\left(c^2 - \Omega_q^2 \frac{\nu^2 J}{A}\right) \gamma_q \sin(\gamma_q L) = -\frac{k_d}{\rho A} \cos(\gamma_q L) \\ \left(c^2 - \Omega_q^2 \frac{\nu^2 J}{A}\right) \frac{\gamma_q \rho A}{k_d} \tan(\gamma_q L) - 1 = 0 \end{gathered} \tag{4-18}$$

And since all the constants (except for Ω_q) in the equation are known, it is possible to numerically find each eigenfrequency Ω_q belonging to each eigenmode $U_{z,q}$. Figure 4-1 shows the first five eigenmodes, following from the above equations.

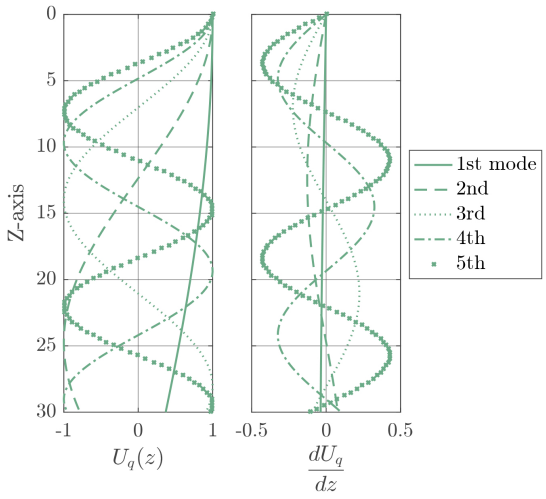

Figure 4-1: The left graph represents the first five eigenmodes of a pile constrained by a spring at the bottom and right graph represents its first derivative

4-2-2 Amplitude factor

The shapes of the eigenmodes are known, hence the amplitude factors can be defined. Substituting Eq. (4-10) into Eq. (4-11), is the first step to find the amplitude factor A_q:

$$\sum_{q=0}^{\infty} A_q \left(\frac{\partial^2 \tilde{U}_q}{\partial z^2} + k_p^2 \tilde{U}_q \right) = B \left(\sum_{q=0}^{\infty} A_q \frac{\nu}{\rho} \tilde{p}_q - \frac{\tilde{F}(\omega)}{\rho A} \delta(z) + i\omega c_d \sum_{q=0}^{\infty} A_q U_q \delta(z-L) \right) \tag{4-19}$$

$$\sum_{q=0}^{\infty} A_q \left(\left(-\gamma_q^2 + k_p^2 \right) \tilde{U}_q - B \left(\frac{\nu}{\rho} \tilde{p}_q + i\omega \frac{c_d}{\rho A} U_q \delta(z-L) \right) \right) = -B \frac{\tilde{F}(\omega)}{\rho A} \delta(z) \tag{4-20}$$

By applying the orthogonality principle of the eigenmodes of the pile, we can find A_q.

$$\int_0^L \left\{ \sum_{q=0}^{\infty} A_q \left(\left(-\gamma_q^2 + k_p^2 \right) \tilde{U}_q - B \left(\frac{\nu}{\rho} \tilde{p}_q + i\omega \frac{c_d}{\rho A} U_q \delta(z-L) \right) \right) = -B \frac{\tilde{F}(\omega)}{\rho A} \delta(z) \right\} U_m dz \tag{4-21}$$

$$\sum_{m=0}^{\infty} A_m \left(\left(-\gamma_m^2 + k_p^2 \right) \int_0^L U_q U_m dz - B \left(\frac{\nu}{\rho} \tilde{p}_{qm} + i\omega \frac{c_d}{\rho A} \int_0^L U_q U_m \delta(z-L) dz \right) \right) = -B \; P_m \tag{4-22}$$

Where

$$\tilde{p}_{qm} = \nu R \frac{2\omega^2 \rho_w}{(z_2 - z_1)} \int_{z_1}^{z_2} U_m \sum_{n=0}^{\infty} Q_n(r, z, \omega) dz \int_{z_1}^{z_2} \frac{\partial U_q}{\partial z} \sin\left(k_{z,n}(z - z_1)\right) dz \tag{4-23}$$

$$P_m = \frac{\tilde{F}(\omega)}{\rho A} \int_0^L U_m \delta(z) dz \tag{4-24}$$

In Eq. (4-23) still both modes q and m are presented. This means that there is a possibility that another mode influences the current mode when $q \neq m$, which is called cross-modal or mutual impedance. When $q = m$ the current mode is only influenced by its own pressure (self-impedance).
For light fluids like air, A_m is often approximated by neglecting the mutual impedances and set the off-diagonal terms to zero. Then:

$$A_m = -\frac{B \cdot P_m}{\left(-\gamma_m^2 + k_p^2\right) \int_0^L U_m^2 dz - B\left(\frac{\nu}{\rho}\tilde{p}_{mm} + i\omega \frac{c_d}{\rho A} \int_0^L U_m^2 \delta(z - L) dz\right)} \tag{4-25}$$

However, water is a heavy fluid and the mutual impedance does have a minor influence around the ring frequency in a model based on the shell theory, according to Tsouvalas [1]. Therefore both cases will be taken into account when finding the actual values of A_m or A_q. A system of linear equations is obtained, to find all amplitude factors A_m or A_q:

$$A_m \left(\left(-\gamma_m^2 + k_p^2\right) \int_0^L U_q U_m dz - B\left(\frac{\nu}{\rho}\tilde{p}_{mm} + i\omega \frac{c_d}{\rho A} U_m^2(L)\right)\right) - \sum_{q=0}^{\infty} A_q B \frac{\nu}{\rho} \tilde{p}_{qm} = -B\ P_m \tag{4-26}$$

4-3 Validation of modal analysis method

To check whether or not the solution of the modal analysis method is correct, this model is compared with the model from Chapter 2. For this purpose, the pressure terms are neglected in the final solution for $\tilde{u}(z, \omega)$ to obtain an uncoupled system. In this case the amplitude factor equals:

$$A_m = -\frac{B \cdot P_m}{\left(-\gamma_m^2 + k_p^2\right) \int_0^L U_m^2 dz - i\omega B \frac{c_d}{\rho A} \int_0^L U_m^2 \delta(z - L) dz} \tag{4-27}$$

As seen in Figure 4-2, both solutions for the longitudinal deformation are similar to each other in time; the deformation of the modal solution is slightly smaller than the deformation of the analytical solution. In frequency domain there is a difference for higher frequencies.
The radial deformation from modal analysis, however, differs from the analytical solution (see Figure 4-3). This difference is caused by the assumption in modal analysis that the first derivative of the top-node is zero, which in reality will not be the case. This assumption has to be considered when using the model in the future.

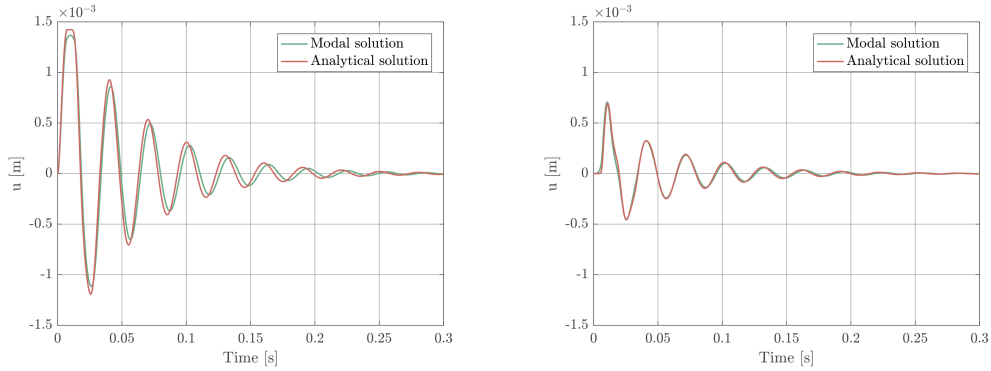

Figure 4-2: Comparison of analytical and modal solution in both frequency and time domain. Figure(a) represents the top-node and figure (b) represents the bottom-node.

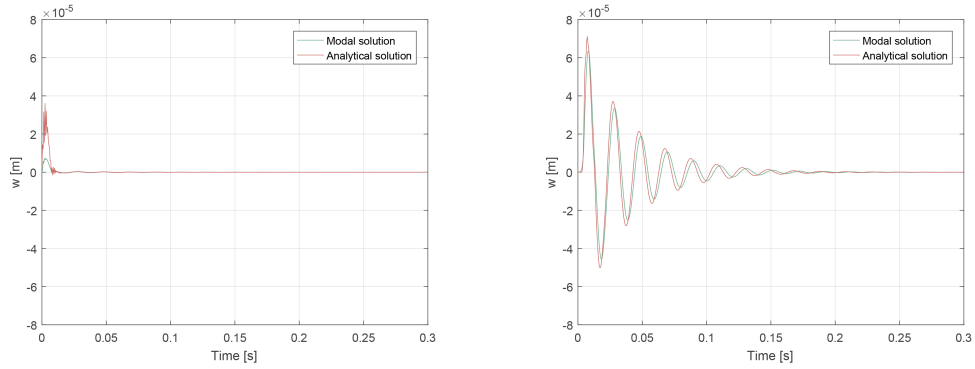

Figure 4-3: Comparison of analytical and modal solution of radial deformation in time domain. Figure (a) presents the radial deformation of the second top-node and Figure (b) of the bottom-node. It is chosen to present the second top-node instead of the first, since the first node is zero in modal domain due to its boundary conditions.

4-4 Differences coupled and semi-coupled model

As shown in the previous section, the modal analysis is consistent with the analytical solution for the semi-coupled model. Based on this, the modal analysis can be used to present and analyse the influence of pressure in the deformation of the pile.

In Figure 4-4 the results of this analysis are presented. In contrast to the hypothesis as described in the introduction of this chapter, the differences between the coupled solution and semi-coupled solution are not visible at first sight. Only when zooming in, these differences are visible. Based on this comparison between the modal solution of the semi-coupled system with the modal solution of the coupled system, one can conclude that the differences between coupled and semi-coupled are smaller than the

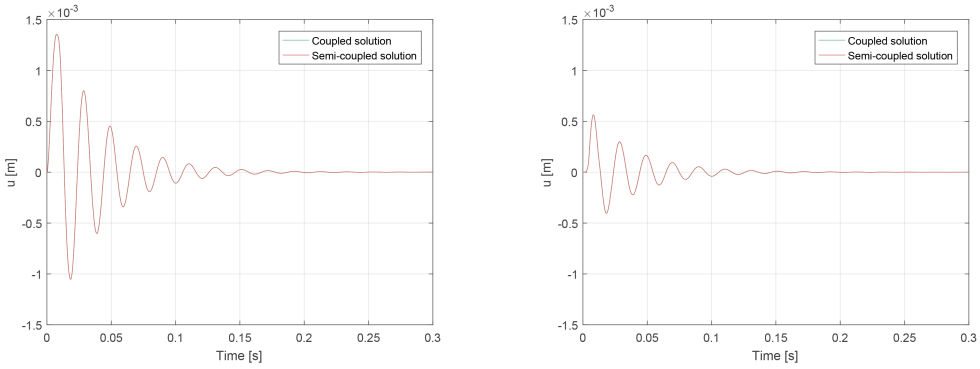

Figure 4-4: Comparison of coupled and semi-coupled solution in time domain. Figure (a) presents the longitudinal deformation of the top-node and Figure (b) of the bottom-node

differences between the modal and analytical analysis. Therefore, it is concluded that the difference between a model with and a model without pressure terms is smaller than the error of the numerical model and it can be assumed that the pressure is negligible in this model. This negligibility can be caused by the fact that the pressure is coupled to the model using the Poisson effect, instead of a full inertia coupling. Due to this method of coupling the factor including the pressure term is relatively small compared to the other terms in Eq. (4-26) and it has only a small influence on the final results. To increase the computational efficiency, the pressure terms in the pile model will therefore be neglected in the following chapters of this document.

4-5 Conclusion

After proposing a model for pile deformations and a model to simulate pressures in surrounding fluids due to the deformations, this chapter describes a method to couple the models, by coupling a pressure term in the equation of motion of the pile. Modal analysis makes it possible to deal with the integral terms in the pressure function. Before adding the pressure term to the equation of motion, the modal method is compared with the analytical method for validation purposes. When comparing the analytical and semi-analytical model, small differences due to different application of the boundary conditions are visible.

After this comparison, the pressure terms are included in the modal analysis model. It appears that the differences between the semi-coupled model from Chapter 2 and the coupled model from this chapter are not visible. Since coupling means a decrease in computational efficiency and including pressure terms does (almost) not differ from neglecting them, the pile model will not be coupled to the fluid pressure, during further research to underwater noise emission.

Chapter 5

Model limitations

In general, any model is a simulation of reality. Furthermore, assumptions and simplifications will lead to uncertainties in the results. This chapter summarizes the limitations of the model described in the previous chapters due to its assumptions and simplifications, as well as the consequences for the results of this thesis are discussed. For this chapter, it is important to keep in mind that the aim of this thesis is to reduce the Sound Peak Levels in the water and that it is assumed that these levels are caused by the first longitudinal wave travelling downwards through the pile directly after a hammer blow.

5-1 1D Pile Model

In Chapter 2 the longitudinal deformations of a pile are modeled as a one-dimensional model by simplifying the pile to a 1D rod. Although a 1D model provides a good understanding about the physics, it also comes with its downsides.

- One rotational mode:
  A 1D equation of motion describes a motion in one direction for both input and output. Hence, it is assumed that the hammer force acts in line with the z-axis of the pile while in reality it is possible that the hammer has a small inclination, as explained in Chapter 2. This inclination would result in an excitation of one or more rotational modes of the pile and an asymmetrical deformation of the pile. In a 1D model the inclination of the force therefore cannot be taken into account and only the first rotational mode will be excited. Since only this mode is taken into account in the 1D model, this model does not give accurate results in terms of deformation amplitudes and asymmetry. However, assuming that the inclination will be very small, it can be assumed that the first mode has the biggest influence on the final solution and therefore the result will be close to reality.

- Frequency dependent damping:
  Using a 1D equation of motion to calculate the longitudinal deformation in frequency results in problems for high frequencies as discussed in Chapter 2. Therefore a frequency dependent damping is introduced to neglect the problematic frequencies in the final solution. However, these (mostly high) frequencies might have a large influence on peak pressures in an acoustic medium and this simplification will decrease the accuracy of the underwater noise levels.

- Soil representation:
  There are different options for the representation of soil and for this thesis it is chosen to use a spring-dashpot system at the bottom of the pile. This means that the waves reflected at the bottom point are not simulated accurately, but for this research this does not influence final results. The evolution of pile deformations to underwater noise due to the first wave travelling down has the main focus of this thesis and therefore it is chosen not to fully model the seabed.

The first two simplifications described above result in a decrease of accuracy of the pile's deformation. However, for this research it is of interest to understand the physics of wave propagation and draw qualitative conclusions with respect to the main question as described in Chapter 1. This means that a decrease in accuracy of the final results will not obstruct the final goal of this thesis, it only limits the possibility to find exact and accurate values for peak pressures.

5-2 Fluid model

Chapter 3 started with discussing the contribution of the three different noise paths to the underwater noise. There was stated that the primary noise path, the path through the water column, is the greatest contributor to underwater noise in most of the cases. Therefore this research focusses on this particular noise path. However, it is also known that the groundborne path may have a big contribution to the underwater noise emission, especially at larger distances when the noise is 'leaking' upwards into the water column. These contributions are not included in this model and the influence of adjusting the piles structure on the waves through the seabed are not checked.

5-3 Coupled model

In Chapter 4 a coupled model was proposed to make the longitudinal deformation of the pile dependent on the fluid pressure, using modal analysis. When comparing this model with the semi-model obtained in Chapter 2, it appeared that (for this model) fluid pressure does not have a significant influence on the deformations, due to the implementation of this term through Poisson's relation instead of implementing it with a full inertia coupling in an equation of motion for the radial deformation. To increase

the computational efficiency it is therefore chosen to continue the research with the semi-coupled model of Chapter 2. For the final solution of the 1D model this has almost no influence and therefore it could safely be assumed that pressure effects can be neglected, but for more complex models one should investigate the influence of pressure on the deformations.

5-4 Conclusion

In this chapter all the assumptions and simplifications used for the model are described. The majority of the simplifications are made in the 1D model. Since this model is an estimate of reality due to all these simplifications, the model will not be validated. It is assumed that, due to implementing multiple aspects of reality (e.g. taking into account the fluid pressure in the pile's deformation), the conclusions of this research will be of qualitative value for the future, but not contain quantitative results. Simplifying this complex problem on the other hand, is more valuable for understanding the physics of a monopile for this research.

Chapter 6

Wave analysis

In the previous chapters, a simplified model for the simulation of pressure waves caused by hammer impact is proposed. This chapter continues the research by analysing the dynamic properties of the monopile and the relation between the propagating waves in the monopile and the fluid pressure, with help from frequency response functions and pressure intensity. This analysis provides insight in the possibilities of placing oscillators, containing mass, stiffness and/or damping, around the monopile to reduce underwater noise levels during pile-driving. It is expected that the oscillators constrain the pile's radial displacement and therefore reduce the perturbation of the surrounding fluid and decrease the noise levels in the water during pile-driving.

This chapter first gives a general explanation of frequency response functions and its use. The explanation is followed by the analysis of the monopile-fluid system, from which conclusions can be drawn regarding the ideal oscillators. From these conclusions the model will be extended with oscillators, in the next chapter.

6-1 Frequency response functions (FRFs)

A frequency response function expresses the relation between the input (in this case the force) and the output (which can be the longitudinal deformation, radial deformation or fluid pressure in this case) in frequency domain. It shows what the eigenfrequencies of the system are, and gives us insight in the stiffness, mass and damping of the system.

A simple mass-spring system (as in Figure 6-1) under harmonic loading is used as an example for better explanation of the FRF and the influence of mass and stiffness on the FRF. Its equation of motion (without damping) is equal to:

$$m\ddot{x} + kx = \hat{F}\cos(\omega t) \tag{6-1}$$

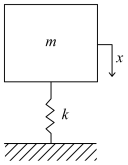

Figure 6-1: A simple mass-spring system

A solution for x can be found in the form of:

$$x(t) = C_1 \sin(\omega t) + C_2 \cos(\omega t) \tag{6-2}$$

The unknown coefficients can be found by substituting $x(t)$ into its equation of motion and make the right hand side and the left hand side equal for each time-moment. This results in:

$$C_1 = 0 \tag{6-3}$$

$$C_2 = \frac{\hat{F}}{k - m\omega^2} \cos(\omega t) \tag{6-4}$$

Then the FRF plots $|\frac{x}{F}|$ and this results in:

$$\left|\frac{x}{F}\right| = \frac{1}{k - m\omega^2} \tag{6-5}$$

The FRF of Eq. (6-5) is plotted in Figure 6-2 in the top left graph. Three different parts in this graph can be seen:

1. $\omega < \sqrt{\frac{k}{m}}$ - Then, as seen in Eq. (6-5), the FRF is approaching $1/k$ (the stiffness-line). This is the first linear part in the plot.

2. $k = m\omega^2$ or $\omega = \sqrt{\frac{k}{m}}$ - When ω reaches this value, the FRF goes to infinity. This explains the peak in the FRF, it represents the first eigenfrequency of the system, ω_0.

3. $\omega > \sqrt{\frac{k}{m}}$ - The mass term takes over and the result of Eq. (6-5) approaches $\frac{1}{-m\omega^2}$. In the graph this is the decreasing line after the peak of the first eigenfrequency.

Figure 6-2 also presents the influence of mass and stiffness on the FRF for a simple system in the bottom left and top right graph respectively. A higher mass results higher eigenfrequency and the other way around, while a higher stiffness results in a lower stiffness line and higher eigenfrequency. Changing the values of k or m, causes the crossing between the two moving left or right, as can be seen in both figures.

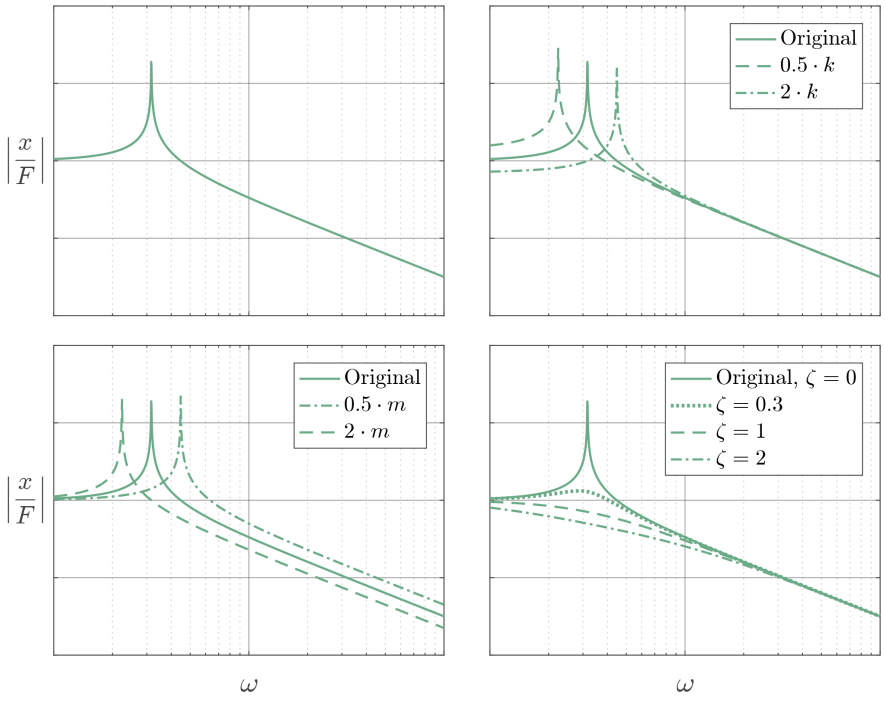

Figure 6-2: The top left figure presents the FRF of the simple mass-spring system, without damping. In the top right figure and bottom left figure the influence of mass and stiffness are plotted respectively. The bottom right figure presents the FRF of a mass-damper-spring system, with different amounts of damping. All figures are plotted in logscale.

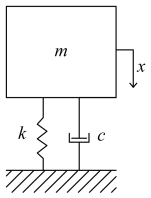

Figure 6-3: A simple mass-spring-damper system

If damping is added to the system, as in Figure 6-3, the equation of motion of a simple system changes to:

$$m\ddot{x} + c\dot{x} + kx = \hat{F}\cos(\omega t) \tag{6-6}$$

With this new equation of motion a new solution for x is found. Its corresponding FRF equals:

$$\left|\frac{x}{F}\right| = \frac{1}{\sqrt{(k - m\omega^2)^2 + (c\omega)^2}} \tag{6-7}$$

The bottom right graph in Figure 6-2 shows that increasing damping will decrease the peak at the eigenfrequency and three damping types are distinguished here:

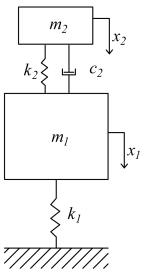

Figure 6-4: Mass-spring system including a Tuned Mass Damper (TMD)

1. Underdamped - when $0 < \zeta < 1$ with ζ as the damping ratio ($\frac{c}{c_{cr}}$). This is the dashed line in the graph in Figure 6-2.
2. Critical damping - when $\zeta = 1$, as seen in the dotted line in the graph in Figure 6-2.
3. Overdamped - when $\zeta > 1$, represented by the dashed-dot line in the graph in Figure 6-2.

When critical damping is reached, there is no peak at the eigenfrequency any more and the graph smoothly transitions from the $1/k$ line (stiffness line) to the $-1/(m\omega^2)$ line (mass line).

6-1-1 Tuned Mass Damper

Besides just adding mass and/or stiffness, it is possible to add a Tuned Mass Damper (TMD). The TMD is tuned to act as a harmonic absorber and reduces the amplitude of structural vibrations. A light component is added to the structure to reduce the intensity of resonances at the eigenfrequencies. The TMD can be explained by a simple system as visualised in Figure 6-4 and described in the following equations:

$$m_1\ddot{x}_1 + c_2(\dot{x}_1 - \dot{x}_2) + k_1x_1 + k_2(x_1 - x_2) = F(t) \tag{6-8}$$

$$m_2\ddot{x}_2 + c_2(\dot{x}_2 - \dot{x}_1) + k_2(x_2 - x_1) = 0 \tag{6-9}$$

Which can also be written as follows:

$$\begin{bmatrix} m_1 & 0 \\ 0 & m_2 \end{bmatrix} \begin{bmatrix} \ddot{x}_1 \\ \ddot{x}_2 \end{bmatrix} + \begin{bmatrix} c_2 & -c_2 \\ -c_2 & c_2 \end{bmatrix} \begin{bmatrix} \dot{x}_1 \\ \dot{x}_2 \end{bmatrix} + \begin{bmatrix} k_1 + k_2 & -k_2 \\ -k_2 & k_2 \end{bmatrix} \begin{bmatrix} x_1 \\ x_2 \end{bmatrix} = \begin{bmatrix} F(t) \\ 0 \end{bmatrix} \tag{6-10}$$

Assuming that $x(t)$ can be found in the form of $x(t) = xe^{i\omega t}$, where x is either x_1 or x_2, the frequency response function can then be determined from:

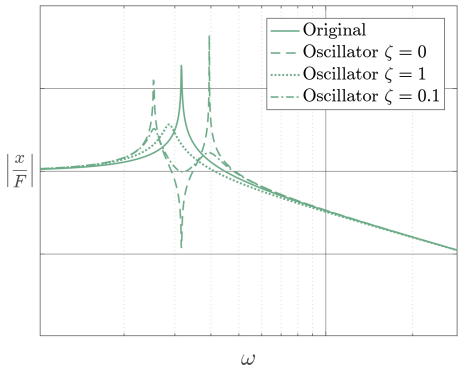

Figure 6-5: Frequency response function of a simple mass spring system including different types of oscillators.

$$\begin{bmatrix} -\omega^2 m_1 + i\omega c_2 + k_1 + k_2 & -i\omega c_2 - k_2 \\ -i\omega c_2 - k_2 & -\omega^2 m_2 + i\omega c_2 + k_2 \end{bmatrix} \begin{bmatrix} x_1 \\ x_2 \end{bmatrix} = \begin{bmatrix} F(t) \\ 0 \end{bmatrix} \tag{6-11}$$

Then the (complex) frequency response function of this system of equations is found as:

$$\frac{x_1}{F} = \frac{-\omega^2 m_2 + i\omega c_2 + k_2}{\left(-\omega^2 m_1 + i\omega c_2 + k_1 + k_2\right)\left(-\omega^2 m_2 + i\omega c_2 + k_2\right) - \left(-i\omega c_2 - k_2\right)^2} \tag{6-12}$$

where the mass m_2 and stiffness k_2 are chosen such that the TMD has the same eigenfrequency as the original mass spring system.
Its result is presented in Figure 6-5. Besides the original function of a simple mass-spring system as described previously, the figure presents three graphs representing three different values for damping c_2. In this figure we can see that adding a TMD without damping results into two new eigenfrequencies and a drop peak at the location of the original eigenfrequency. From this FRF it can be concluded that adding a TMD with a small damping ratio (hence, where $\zeta < 1$), the TMD causes anti-resonance in the system which constrains the system to vibrate at the specific eigenfrequency. When $\zeta \geq 1$, we see that the peak of the eigenfrequency reduces significantly and slightly moves to a lower frequency.

6-1-2 Summary

The above information on FRFs and the use of mass, stiffness and damping, will be used for this research to determine the most effective parameter (or combination of parameters) to be adjusted as described before. Below, an overview of each option is given:

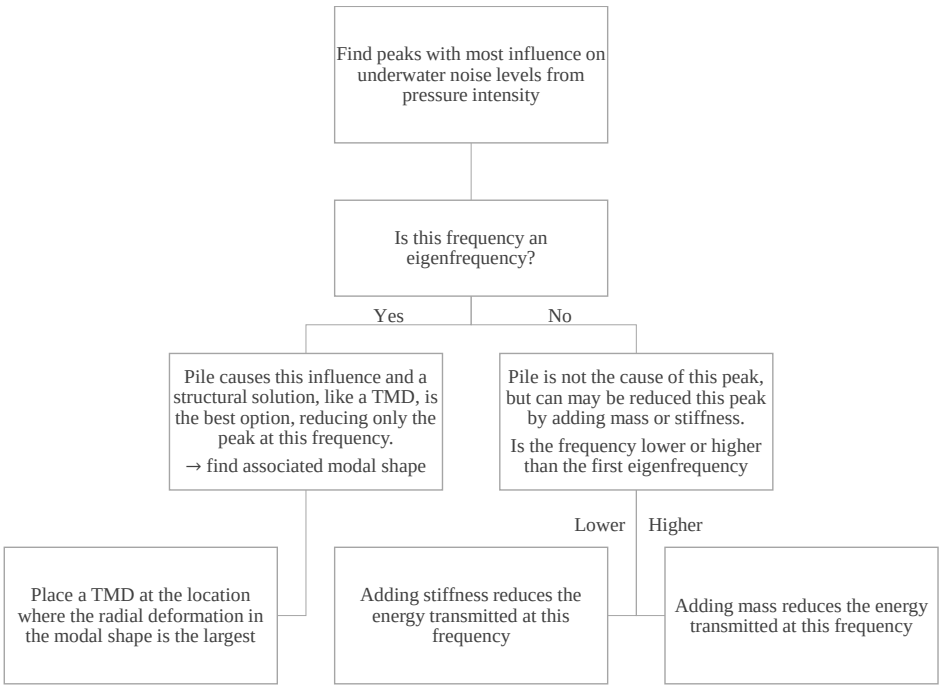

Figure 6-6: The flowchart in this figure presents the steps to follow during the analysis, in order to find the most efficient way to reduce the noise.

1. Adding mass lowers the eigenfrequency and the mass line

2. Adding stiffness lowers the stiffness line and increases the eigenfrequency

3. Adding damping reduces the peak at the eigenfrequency

4. Adding a TMD reduces the amplitude of the eigenfrequencies, due to anti-resonance

In the analysis of FRFs, these FRFs also have to be compared with the force in frequency domain. The force contains its most energy over a limited range of frequencies. Knowing that the final deformation in frequency domain equals the FRF multiplied by the force in frequency domain, this information of force energy contributes to this research when finding out which frequency bands are most effective to adjust.

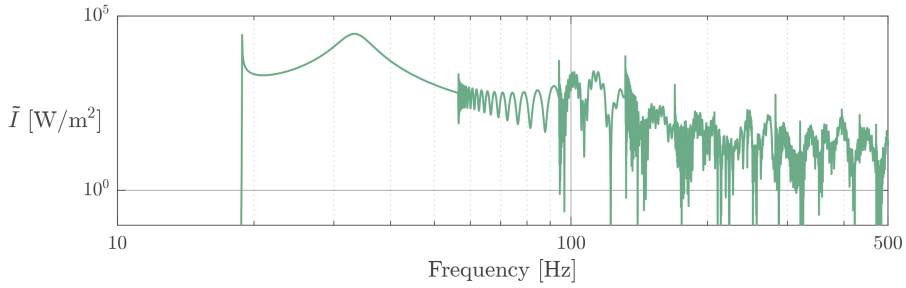

Figure 6-7: Pressure intensity graph in frequency domain. This graph presents for which frequencies the power of the system is the highest and therefore influence the noise levels the most.

6-2 System analysis

The previous section briefly explained the frequency response function and its functionalities. This section continues with the analysis of the monopile under impact loading and its influence on fluid pressure, considering the knowledge of the previous section. This is done by analysing the pressure intensity in frequency domain (Section 6-2-1), finding frequencies with the biggest influence on the noise levels, and the FRFs of the research model (Section 6-2-2) from which the characteristics of these peaks are found, according to the flowchart from Figure 6-6. The parameters and their values used for this model are described in Table 6-1.

Pile					**Water**			
Length	L	30	m		Surface level	z_1	10	m
Diameter	D	5	m		Seabed level	z_2	30	m
Wall thickness	h	70	mm		Mass density	ρ_w	1025	kg/m^3
Young's Modulus	E	210	GPa					
Mass density	ρ	7850	kg/m^3					
Poisson's ratio	ν	0.3						

Table 6-1: Overview of all parameters in the model

6-2-1 Pressure intensity

In this section, the pressure intensity is analysed. Intensity describes the power per unit area [W/m^2], with the area is measured perpendicular to the direction of propagation of energy. This intensity can be calculated as follows:

$$\mathbf{I}(r,z,t) = p(r,z,t) \cdot \mathbf{v}(r,z,t) \tag{6-13}$$

where $\mathbf{v}$ is the particles speed (a vector since it consists of speed in r-direction and speed in z-direction) and p is the pressure at the location of the particle. Since for

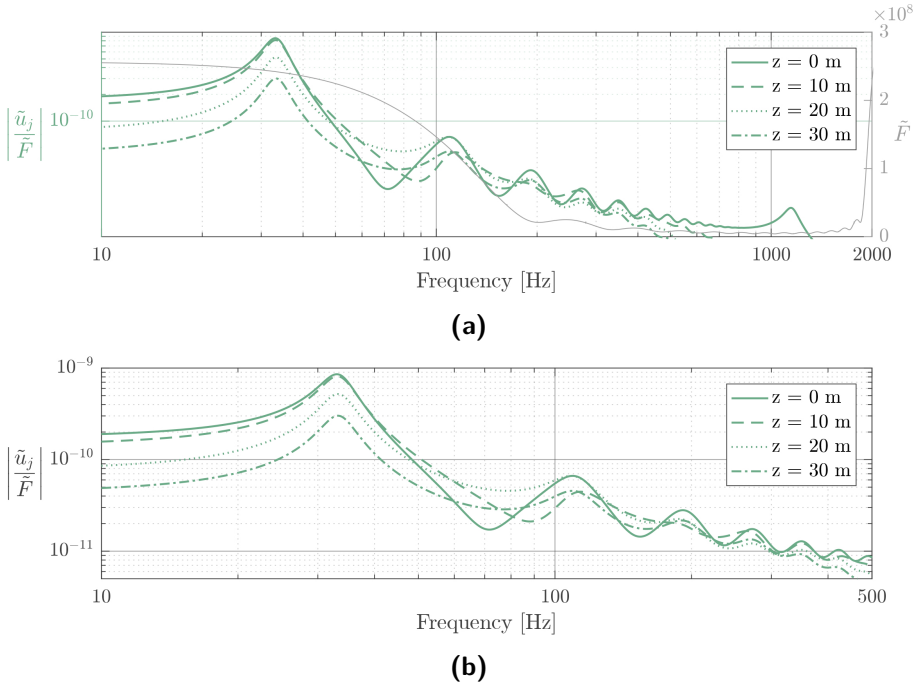

Figure 6-8: Frequency response functions of the longitudinal deformations from different heights. Figure (a) includes both the FRF of these longitudinal deformations and the frequency spectrum of the impact force. Figure (b) focusses on the longitudinal deformations from 10 Hz to 500 Hz only.

this research the energy propagates mostly in radial direction, the intensity in radial direction, measured at 750 m from the pile wall and 5 m above seabed, is analysed and plotted in frequency domain in Figure 6-7.

From this graph, it can be seen that two peaks contain the most power per square meter: a sharp peak at approximately 20 Hz, from where on also the intensity increased significantly, and one less sharp one at approximately 30 Hz. The frequency response functions (FRFs) will provide information of these peaks: if they are eigenfrequencies or not and how it is possible to reduce these peaks only, with the least influence on other dynamic characteristics.

6-2-2 Frequency response functions of model

Besides the pressure intensity, the frequency response functions are analysed, in order to gain information about the peaks found in the previous section.

The main goal of this research is to achieve noise reduction by adjusting the pile's structural dynamics. The noise levels are determined by the pressure levels of the water and thus the FRF of fluid pressure contains information on how the pressures relate to frequency. Adjusting the pile's structural dynamics influences the longitudinal deformation (and additionally the radial deformation). Therefore, the FRF on longitudinal

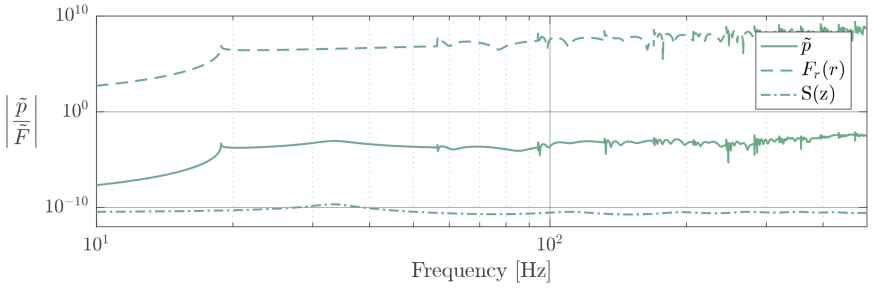

Figure 6-9: Frequency response function of the pressure.

deformation gives a first insight on which parameters to change. The values of each parameter, used in the model, are depicted in Table 6-1.

Figure 6-8a presents the FRF of the longitudinal deformation and the impact force in frequency domain up to a frequency of 2 kHz. The critical frequency (the frequency where wavenumber k_p is infinite, as discussed in Section 2-6-1) is clearly visible just after 1 kHz, with the graphs going to zero. As shown in this figure, the impact force contains the most energy up to approximately 200 Hz, confirming why in the previous section only the lower frequencies from the graph in Figure 6-7 contain the most power.

Figure 6-8b zooms in at the FRF of the longitudinal deformation up to 500 Hz. Here it can be seen that the FRF for different nodes are quite similar, only after the first peak (representing the first eigenfrequency) differences occur due to viscous damping at the bottom. Note that the frequency depended damping is not included in the FRFs to get a clearer view on the eigenfrequencies of the system.

Comparing this FRF with the intensity graph of the previous section, it can be concluded that the second peak in the intensity graph equals the first eigenfrequency of the pile. Following the flowchart, it is convenient to reduce the peak of this eigenfrequency using a TMD. Using damping or to move the eigenfrequency to a frequency outside the "energy" region by adding stiffness will also affect other frequencies, and is therefore not preferred.

Secondly, it is important to analyse the FRF of the pressure, presented in Figure 6-9, since it is the pressure that needs to be reduced to lower underwater noise levels. Here, one can see that the cut-off frequency (as explained in Section 3-3) is visible; below 18 Hz the FRF is almost zero (here the pressure contains almost no energy) and at the cut-off frequency the amplitude increases significantly (energy increase). The first peak as seen in the intensity graph in Figure 6-7 is caused by this cut-off frequency.

Additional to the FRF of the pressure itself, it is useful to know how this change of the longitudinal deformation[1] influences the pressure. Therefore, this figure also includes

[1] A note has to be made here; pressure is influenced by the radial deformation. However, the radial deformation, on its turn, depends on longitudinal deformation. The model for longitudinal deformation is not coupled to the radial deformation, therefore the only possibility to influence pressure is by changing the longitudinal deformation by adding oscillators which constrain the pile in radial direction using Poisson's ratio.

$F(r)$ and $S(z)$, the two terms defining $\tilde{p}$ when multiplied (see Chapter 3). $F(r)$ defines the radial propagation through fluid and $S(z)$ the propagation along the z-axis. As can be read in Section 3-3, only $S(z)$ depends on the deformation of the pile. This relation is also visible in the figure: the FRF of $S(z)$ follows the FRF of $\tilde{u}$, while $F(r)$ shows an entirely different behaviour. From these facts, one can conclude that changes in the FRF of $\tilde{u}$ are only visible in the FRF of $S(z)$ and that these changes are only useful for reducing the underwater noise emission after the cut-off frequency. Comparing the two parts in the FRF of $\tilde{p}$ in Figure 6-9, one can see that $F(r)$ increases exponentially from the cut-off frequency, while $S(z)$ decreases exponentially only after the first eigenfrequency, counterbalancing the increasing $F(r)$.

The cut-off frequency itself cannot be changed, since it is only dependent on the water depth and not directly influenced by the pile. However, it is possible to reduce the influence of the noise levels, by adding stiffness (this frequency is below the first eigenfrequency of the pile and therefore adding mass does not influence this specific frequency). Adding stiffness lowers the "stiffness-line" of the pile's longitudinal deformation and therefore also lowers the first part of $S(z)$. From Figure 6-8a, it can be concluded that the top node has the biggest response. This means that adjusting the top of the pile will influence the final results the most and therefore stiffness has to be added at the top of the pile.

6-3 Conclusion

In this chapter, the relation between the impact load on a monopile and the noise levels in the surrounding fluid are investigated, by means of pressure intensity and frequency response functions. This analysis provided information on how to apply an oscillator and which parameters have to be included. From this analysis it is concluded that the cut-off frequency from the fluid and the first eigenfrequency of the pile contain the most energy and therefore cause the highest pressure levels in the water. A Tuned Mass Damper (TMD) is proposed to reduce the influence of the first eigenfrequency. However, since the cut-off frequency is caused by the pile, a TMD will not reduce this peak. Adding stiffness to the pile is expected to reduce the effect of the cut-off frequency and therefore he next chapter continues the research by implementing a TMD the first eigenfrequency of the pile and extra stiffness to reduce the effect of the cut-off frequency.

Chapter 7

Results

From the previous chapter it was concluded to add Tuned Mass Dampers (TMDs) along the pile to reduce the influence of the first eigenfrequency of the pile and the influence of the first eigenfrequency of the fluid. First, a TMD is added to the model of the monopile, in the following section. Then, it is possible to investigate the optimal values for a TMD for the current case and presents the final results of the thesis.

7-1 Adding a TMD to the model

The inclusion of oscillators (in this case a TMD) requires a new equation of motion. Using Dirac-delta functions provides the opportunity to apply oscillators at different levels. Then the new equation of motion becomes:

$$c^2\frac{\partial^2 u}{\partial z^2} - \frac{\partial^2 u}{\partial t^2} + \frac{\nu^2 J}{A}\frac{\partial^2}{\partial t^2}\left(\frac{\partial^2 u}{\partial z^2}\right) = \left(\frac{k_{tmd}}{\rho A}(w_{tmd} - w) + \frac{c_{tmd}}{\rho A}(\dot{w}_{tmd} - \dot{w})\right)\delta(z - z_{tmd}) \tag{7-1}$$

$$m_{tmd}\ddot{w}_{tmd} + c_{tmd}(\dot{w}_{tmd} - \dot{w}) + k_{tmd}(w_{tmd} - w) = 0 \tag{7-2}$$

where z_{tmd} is the location along the z-axis of the TMD and w_{tmd} is the deformation of the mass of the TMD.

The equation of motion of the monopile transforms easily into frequency domain using the Fourier transform from Eq. (2-29), resulting in:

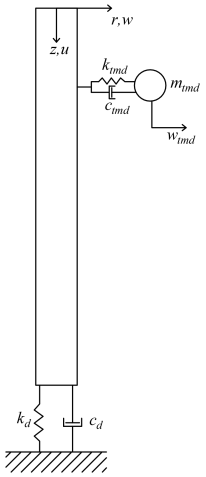

Figure 7-1: Schematic model of monopile, including a Tuned Mass Damper

$$c^2\frac{\partial^2\tilde{u}}{\partial z^2}+\omega^2\tilde{u}-\omega^2\frac{\nu^2 J}{A}\frac{\partial^2\tilde{u}}{\partial z^2}=\left(\frac{k_{tmd}}{\rho A}(\tilde{w}_{tmd}-\tilde{w})+i\omega\frac{c_{tmd}}{\rho A}(\tilde{w}_{tmd}-\tilde{w})\right)\delta(z-z_{tmd}) \tag{7-3}$$

$$\frac{\partial^2\tilde{u}}{\partial z^2}+k_p^2\tilde{u}=B(\omega)\left(\frac{k_{tmd}}{\rho A}(\tilde{w}_{tmd}-\tilde{w})+i\omega\frac{c_{tmd}}{\rho A}(\tilde{w}_{tmd}-\tilde{w})\right)\delta(z-z_{tmd}) \tag{7-4}$$

where

$$k_p=\sqrt{\frac{\omega^2}{c^2-\omega^2\frac{\nu^2 J}{A}}} \tag{7-5}$$

$$B(\omega)=\frac{k_p^2}{\omega^2} \tag{7-6}$$

And the same holds for the equation of motion of the TMD, from which $\tilde{w}_{tmd}$ can be defined:

$$-\omega^2 m_{tmd}\tilde{w}_{tmd}+i\omega c_{tmd}(\tilde{w}_{tmd}-\tilde{w})+k_{tmd}(\tilde{w}_{tmd}-\tilde{w})=0 \tag{7-7}$$

$$\tilde{w}_{tmd}\left(-\omega^2 m_{tmd}+i\omega c_{tmd}+k_{tmd}\right)-\tilde{w}\left(i\omega c_{tmd}+k_{tmd}\right)=0 \tag{7-8}$$

$$\tilde{w}_{tmd}=\xi\tilde{w} \tag{7-9}$$

with

$$\xi=\frac{i\omega c_{tmd}+k_{tmd}}{-\omega^2 m_{tmd}+i\omega c_{tmd}+k_{tmd}} \tag{7-10}$$

Then Eq. (7-4) can be rewritten as:

$$\frac{\partial^2 \tilde{u}}{\partial z^2} + k_p^2 \tilde{u} = B(\omega) \left(\frac{k_{tmd}}{\rho A} + i\omega \frac{c_{tmd}}{\rho A} \right) \tilde{w}(\xi - 1)\delta(z - z_{tmd}) \tag{7-11}$$

Using the relation between the radial deformation $\tilde{w}$ and the longitudinal deformation $\tilde{u}$ from Eq. (2-17) gives:

$$\frac{\partial^2 \tilde{u}}{\partial z^2} + k_p^2 \tilde{u} = -B(\omega) \left(\frac{k_{tmd}}{\rho A} + i\omega \frac{c_{tmd}}{\rho A} \right) \nu R \frac{\partial \tilde{u}}{\partial z}(\xi - 1)\delta(z - z_{tmd}) \tag{7-12}$$

Using modal analysis, as is done in Chapter 4, the equation of motion (including force at the top of the pile and the viscous damping at the bottom of the pile, as in Eq. (7-13)) can be readily solved. The eigenmodes are equal with the eigenmodes from Chapter 4. The only difference is the value for the amplitude factor A_m, due to the addition of the mass and stiffness along the pile (for the sake of simplicity, the addition of damping is left out of the scope of this thesis).

$$\begin{aligned} \frac{\partial^2 \tilde{u}}{\partial z^2} + k_p^2 \tilde{u} = B(\omega) \Bigg(& -\frac{\tilde{F}(\omega)}{\rho A}\delta(z) - i\omega \frac{c_d}{\rho A}\tilde{u}\ \delta(z - L) \\ & - \left(\frac{k_{tmd}}{\rho A} + i\omega \frac{c_{tmd}}{\rho A} \right) \nu R \frac{\partial \tilde{u}}{\partial z}(\xi - 1)\delta(z - z_{tmd}) \Bigg) \end{aligned} \tag{7-13}$$

As in Chapter 4, modal analysis is used to find a solution for (7-13), hence a solution in the form of Eq. (4-10) can be found.

$$\tilde{u}(z, \omega) = \sum_{q=0}^{\infty} A_q U_q(z) \tag{4-10}$$

Since the boundary conditions are similar to the ones from Chapter 4, the same solution for the eigenmodes U_q is found:

$$U_q(z) = \cos(\gamma_q z) \tag{7-14}$$

Substituting the above equations in Eq. (7-13) gives:

$$\begin{aligned} \sum_{q=0}^{\infty} A_q \Bigg\{ & \left(-\gamma_q^2 + k_p^2 + B(\omega) i\omega \frac{c_d}{\rho A}\delta(z - L) \right) U_q \\ & + B\nu R \left(\frac{k_{tmd}}{\rho A} + i\omega \frac{c_{tmd}}{\rho A} \right) \frac{dU_q}{dz}(\xi - 1)\delta(z - z_{tmd}) \Bigg\} = -B \frac{\tilde{F}(\omega)}{\rho A}\delta(z) \end{aligned} \tag{7-15}$$

The orthogonality principle of the modes can be used to find A_q:

$$\int_0^L \left\{ \sum_{q=0}^{\infty} A_q \left\{ \left(-\gamma_q^2 + k_p^2 + B(\omega) i\omega \frac{c_d}{\rho A} \delta(z-L) \right) U_q \right. \right. \\ \left. \left. + B\nu R \left(\frac{k_{tmd}}{\rho A} + i\omega \frac{c_{tmd}}{\rho A} \right) \frac{dU_q}{dz} (\xi - 1) \delta(z - z_{tmd}) \right\} = -B \frac{\tilde{F}(\omega)}{\rho A} \delta(z) \right\} U_q dz \tag{7-16}$$

This results in:

$$A_m \left(I_m + B(\omega) C_m + B(\omega) K_m \right) + \sum_{q=0}^{\infty} A_q B(\omega) K_{qm} = -B(\omega) P_m \tag{7-17}$$

where

$$I_m = \left(-\gamma_m^2 + k_p^2 \right) \int_0^L U_m^2 dz \tag{7-18}$$

$$C_m = i\omega \frac{c_d}{\rho A} U_m^2(L) \tag{7-19}$$

$$K_m = \nu R \left(\frac{k_{tmd}}{\rho A} + i\omega \frac{c_{tmd}}{\rho A} \right) (\xi - 1) \int_0^L \frac{dU_m}{dz} U_m \delta(z - z_{tmd}) dz \tag{7-20}$$

$$K_{qm} = \nu R \left(\frac{k_{tmd}}{\rho A} + i\omega \frac{c_{tmd}}{\rho A} \right) (\xi - 1) \int_0^L \frac{dU_q}{dz} U_m \delta(z - z_k) dz \tag{7-21}$$

$$P_m = \frac{\tilde{F}(\omega)}{\rho A} \int_0^L U_m(z) \delta(z) dz \tag{7-22}$$

Here the same phenomenon as found in Chapter 4 occurs; there is a possibility that other modes influence the current mode (mutual impedance) due to the stiffness, which constrains the radial direction.

7-2 Results

The model is extended with the possibility to add a Tuned Mass Damper and oscillators and the influence of them is investigated in this section in different steps:

1. First investigate the influence of one TMD, reducing the peak of the first eigenfrequency of the monopile and investigate the influence of the weight (and stiffness) of the TMD;

2. Then add extra stiffness in an oscillator at the top of the pile, reducing the peak of the cutoff frequency of the fluid and investigate the influence of different stiffnesses of this oscillator;

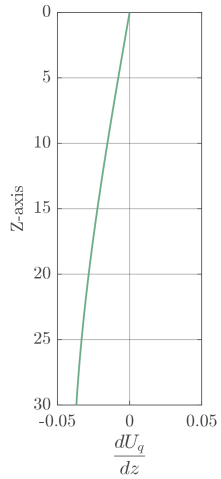

Figure 7-2: First eigenmode of the radial deformation in modal analysis

3. Last, the influence of damping is researched, damping is added in different values.

In order to observe and analyse the results equally, the following aspects are checked:

1. FRFs of longitudinal deformation and pressures;
2. Steepness of the wave front;
3. Reduction of noise levels in the Sound Pressure Levels (SPL);
4. Influence on pile-driveability based on the longitudinal deformation of the bottom node.

7-2-1 Results of adding a TMD

This section investigates the influence of adding one Tuned Mass Damper, to reduce the influence of the first eigenmode at the first eigenfrequency. From Figure 7-2 we know that the amplitude of the first eigenmode is largest at the bottom of the pile. Therefore the TMD has to be placed at the bottom, to increase its influence. For this investigation, damping is not included in the TMD and mass varies from 10% of the monopile's weight up to 100% of the monopiles weight as a theoretical investigation. Since the TMD has to have the same eigenfrequency as the first eigenfrequency of the monopile, stiffness varies too according the following relation:

$$k_{tmd} = m_{tmd}(\omega_{0,p})^2 \tag{7-23}$$

where $\omega_{0,p}$ equals the first eigenfrequency of the monopile and m_{tmd} is the weight of the TMD.

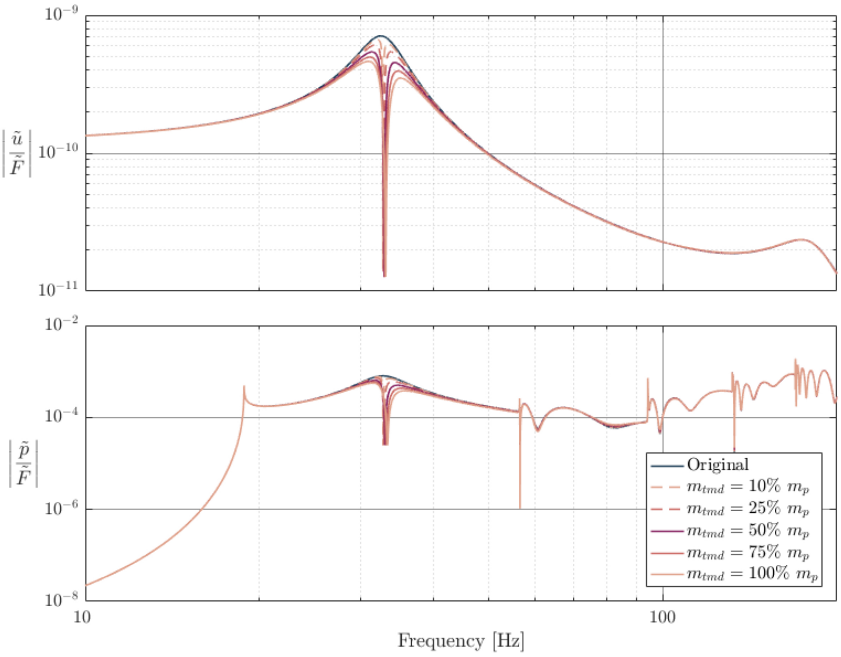

Figure 7-3: Frequency response functions of the system with two TMDs, for different weights of the second TMD.

Figure 7-3 presents the frequency response functions of the longitudinal deformation, radial deformation and pressure, with the TMDs with varying masses (and therefore also varying stiffnesses). In this figure, one can see that an increased mass and stiffness also increases the influence of the TMD on the pressure. Additionally, it can be seen from the top graph that the amplitudes of the longitudinal deformations decreased, due to the additional TMD. It is then expected that the longitudinal deformations in time domain also have a smaller amplitude when a TMD is used, compared to the original situation.

The top graph in Figure 7-4 confirms the expectation that the amplitudes decreased when a TMD is added to the pile. This also means that the pile-driveability might be affected, since the amplitudes of the bottom node are smaller than in the original system. It has also to be noted that the smaller the mass of the TMD, the less influence the TMD has on the amplitudes of the longitudinal deformation.

In the second graph of Figure 7-4, we see the radial deformation of the pile wall. As the goal of this thesis is to reduce noise levels in the water, by means of adding oscillators to change the steepness of the wave front, this graph provides information about this relationship. The graph shows the TMD starts to influence the waves when they reach the bottom, where the TMD is located. The front of the first wave travelling down, therefore, is only influenced in these last seconds when it reaches the bottom. This explains why the decrease of the peaks in the pressure and SPL graphs is small.

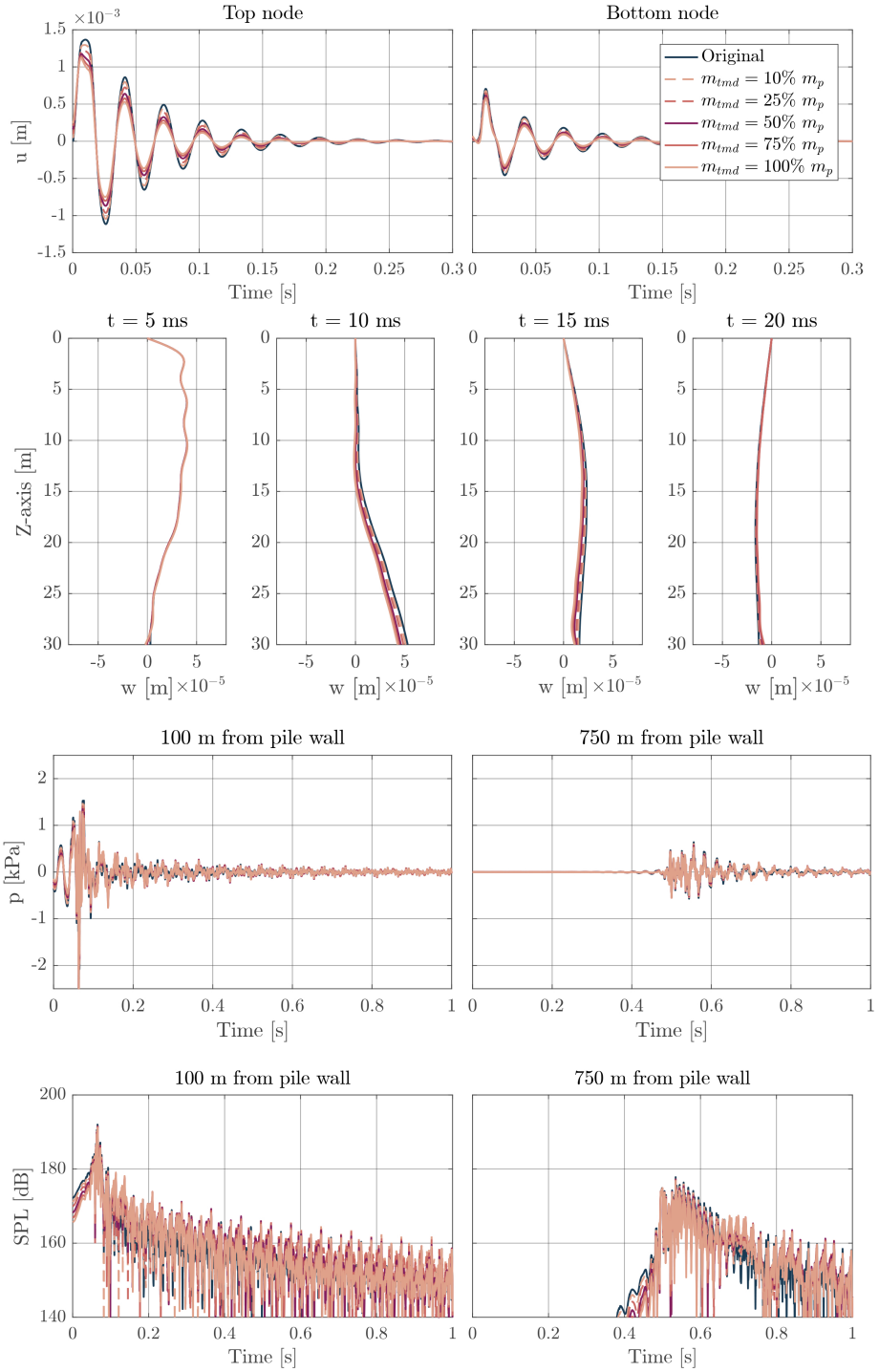

Figure 7-4: Comparison between original system and use of two TMD on longitudinal deformation, pressure levels and SPLs. The weight of the TMD varies and as can be seen the more weight is used, the more the amplitude decreases in each graph.

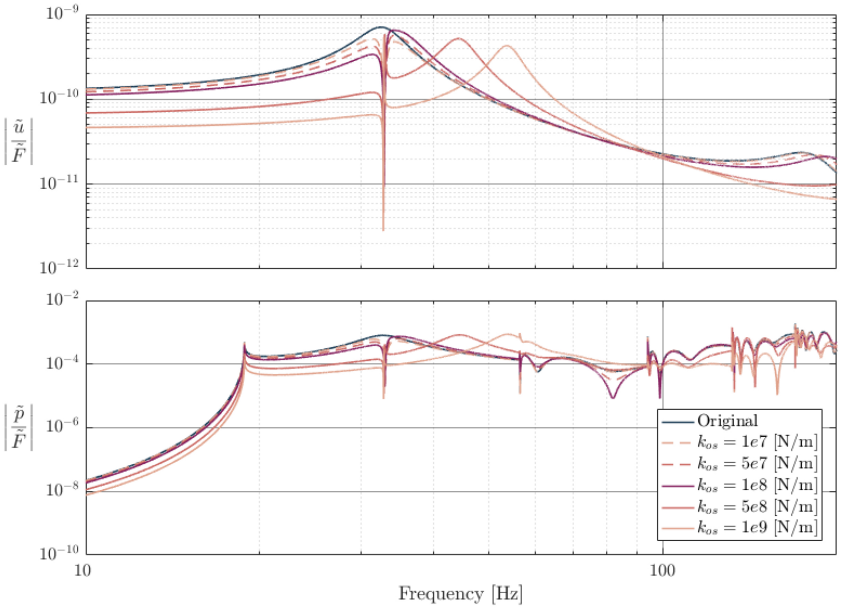

Figure 7-5: Frequency response functions of the system a TMD and added stiffness.

7-2-2 Results of adding stiffness

Now that the influence of adding a TMD for the first eigenfrequency is known, it is interesting to research the influence of adding stiffness to reduce the fluids cut-off frequency.

For this case study, the weight of the first TMD is fixed at half the mass of the monopile. This makes it possible to investigate the influence of a varying stiffness in combination with the TMD.

From the frequency response functions in Figure 7-5, it can be seen that adding stiffness in order to reduce the effect of the peak in the longitudinal deformation FRF at the cut-off frequency, indeed lowers the stiffness-line. Furthermore, adding stiffness affects more frequencies besides the cut-off frequency and it results in a higher eigenfrequency. Due to this, its peak is no longer affected by the TMD, when the difference in eigenfrequency between the pile and TMD is too large. Therefore it is recommended that when both extra stiffness and a TMD are used, the TMD is tuned to the new eigenfrequency of the system.

Figure 7-6 provides results of adding an oscillator with stiffness in time domain. In the top figure where longitudinal deformation is presented, we can see that both the amplitudes and the period has decreased, meaning that the pile-driveability is affected by adding stiffness. Furthermore, it can be seen that the higher the stiffness of the oscillator, the more influence the oscillator has on the final results.

The second graph in Figure 7-6 shows that adding stiffness reduces the amplitudes

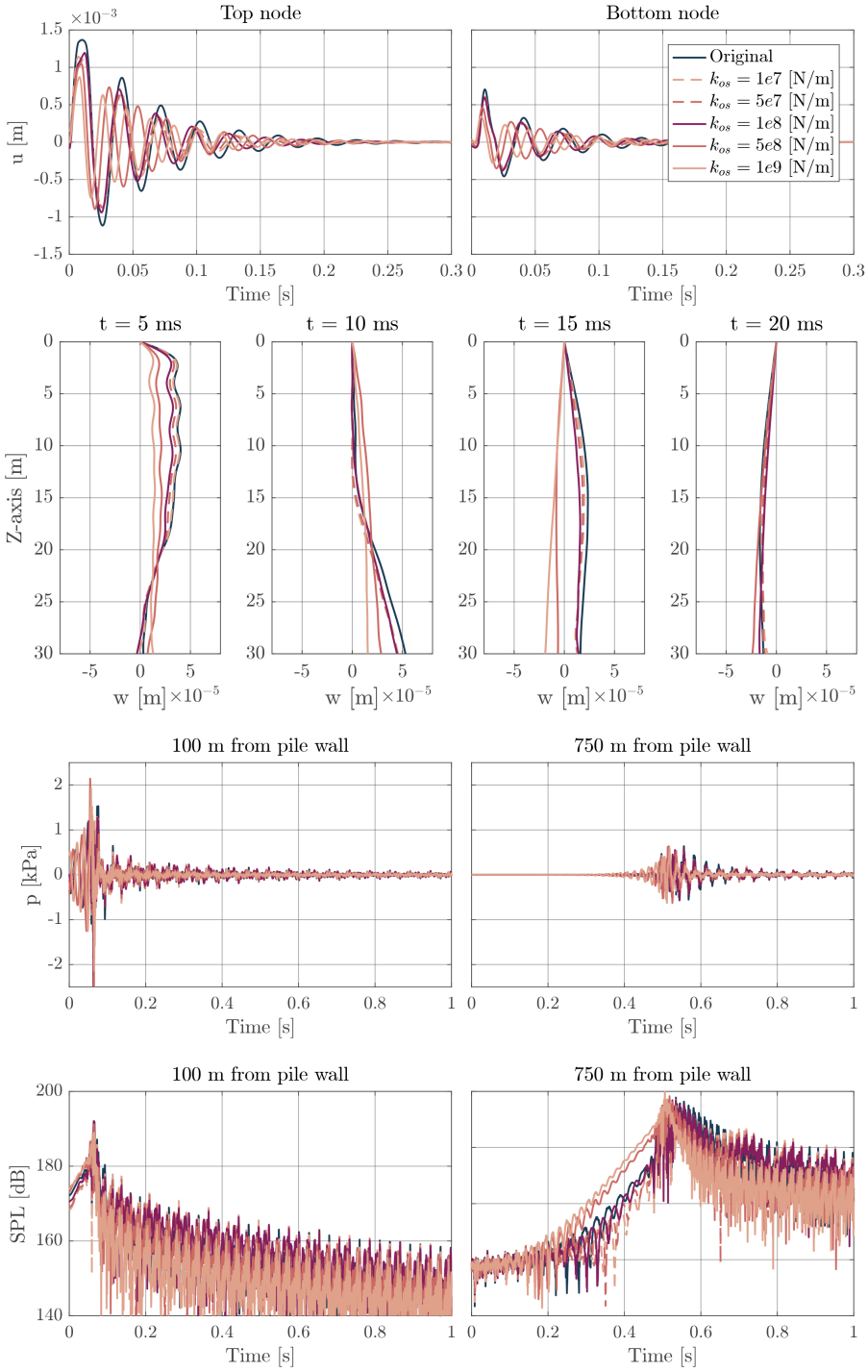

Figure 7-6: Comparison between original system and use of a TMD combined with an oscillator containing stiffness on longitudinal deformation, pressure levels and SPLs. The first TMD applied in this figure has a weight of 0.5 times the weight of the monopile and is located at the bottom of the pile to reduce the first eigenfrequency and eigenmode of the pile. The oscillator is placed at the top of the pile and it's stiffness varies from $1e7$ [N/m] up to $1e9$ [N/m]. As can be seen in the figures the the stiffness increases the eigenfrequency and reduces the effect of the TMD. In the case of a really high stiffness it even cancels the use of both a stiffness and the TMD and the pressures and noise levels are larger than for the original system.

of the radial deformation and therefore also reduces the steepness of the wave front. However, as could already be seen in the top figures, adding stiffness decreases the period of the waves. Due to the decrease of the amplitudes of the deformations, the pile wall moves faster from a positive amplitude to a negative amplitude compared to the original system. This phenomenon is clearly visible in the plots at 10 and 15 ms. Due to this fast transition from plus to minus, one can expect that the pressures are higher than in the original system. This is indeed confirmed in the figures of the pressure and the sound pressure levels, were the higher stiffnesses have higher peaks compared to the system without stiffness. Due to the movement of the first eigenfrequency, the small increasing of its peak and the inability of the TMD to reduce the peak on this new eigenfrequency, a higher stiffness causes even more noise compared to the original system. This confirms the previous thought that when a relatively high stiffness is added, the TMD has to be tuned to the new eigenfrequency of the total stiffness in order to reduce the noise.

7-2-3 Results of using damping

As an additional study, this section investigates the option of adding damping only to the pile. Damping is added in different damping ratios, considering:

$$\zeta = \frac{c}{c_{ref}} \tag{7-24}$$

$$\text{whith} \quad c_{ref} = 2\sqrt{\omega_0^2 m^2} \tag{7-25}$$

where ω_0 equals the first eigenfrequency of the monopile and m is the weight of the monopile. ζ is the damping ratio, but since the damping is applied on the pile in radial direction, ζ has to have a higher order of magnitude compared with a situation where damping is implemented in the same direction as the governing deformation. For this case, the following theoretical values for ζ are used: 2.5, 5, 10, 15 and 20.

Figure 7-7 presents the frequency response functions of the longitudinal deformation and pressure after adding damping at the top of the pile. This graph shows that damping influences a broader frequency spectrum compared to a TMD and increases when frequency increases. Increasing the damping ratio also increases its effect on the deformations and pressures.

Figure 7-8 presents the results in time domain. The top figures show that longtudinal deformation is affected by damping; the amplitudes decrease slightly and its period increase. Due to the period increase and the amplitude decrease, the slope of the wave front is less steep compared to the system without an oscillator, as seen in the second graphs from the top. As a result of this, the peaks of both pressure and sound pressure levels have decreased and we can conclude that damping reduces noise levels.

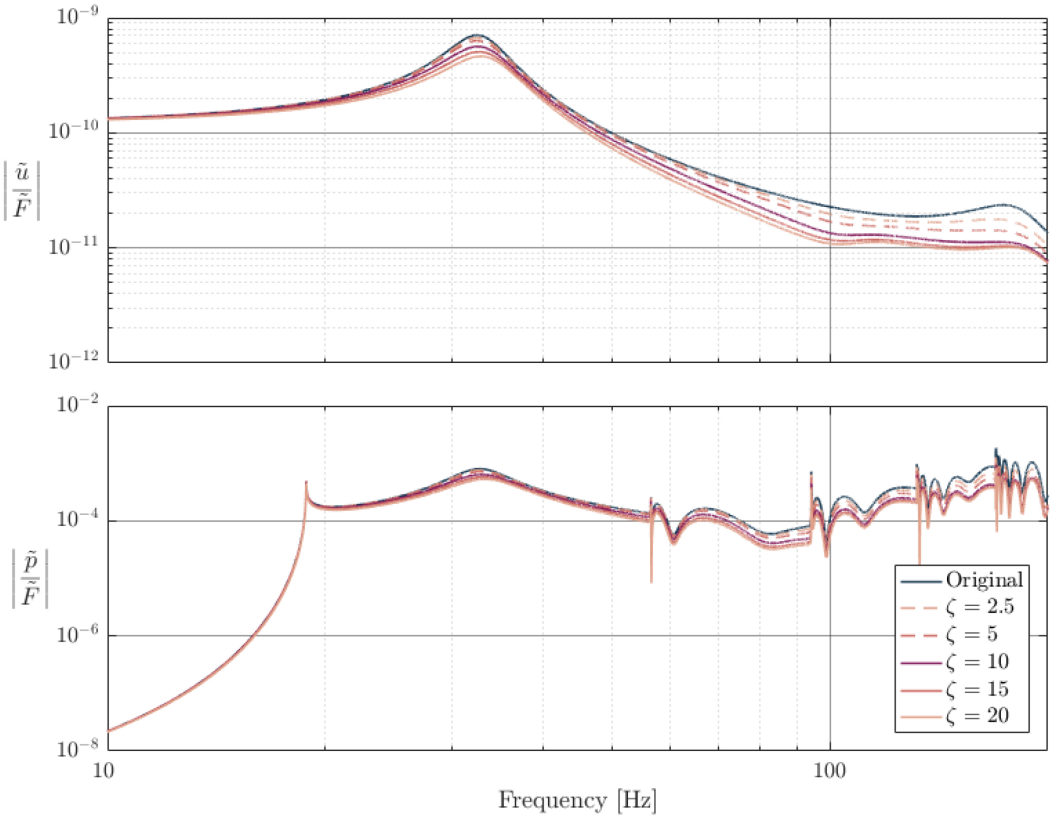

Figure 7-7: Frequency response functions of the system with added damping.

7-3 Conclusion

This chapter studied three options to reduce the underwater noise levels:

1. A Tuned Mass Damper (TMD) to reduce the influence of the first eigenfrequency of the pile only
2. An oscillator containing stiffness, to reduce the influence of the cut-off frequency
3. An oscillator containing damping, to reduce the amplitudes over a broader frequency spectrum

Figure 7-9 gives an overview of the studies performed in this chapter.

From the first study, adding one TMD with varying masses and stiffnesses, it can be concluded that adding a TMD to reduce the influence of the first eigenfrequency does reduce noise levels moderately in the surrounding water. Increasing mass and stiffness will increase the final noise reduction, however, it also increasingly affects the pile-driveability.

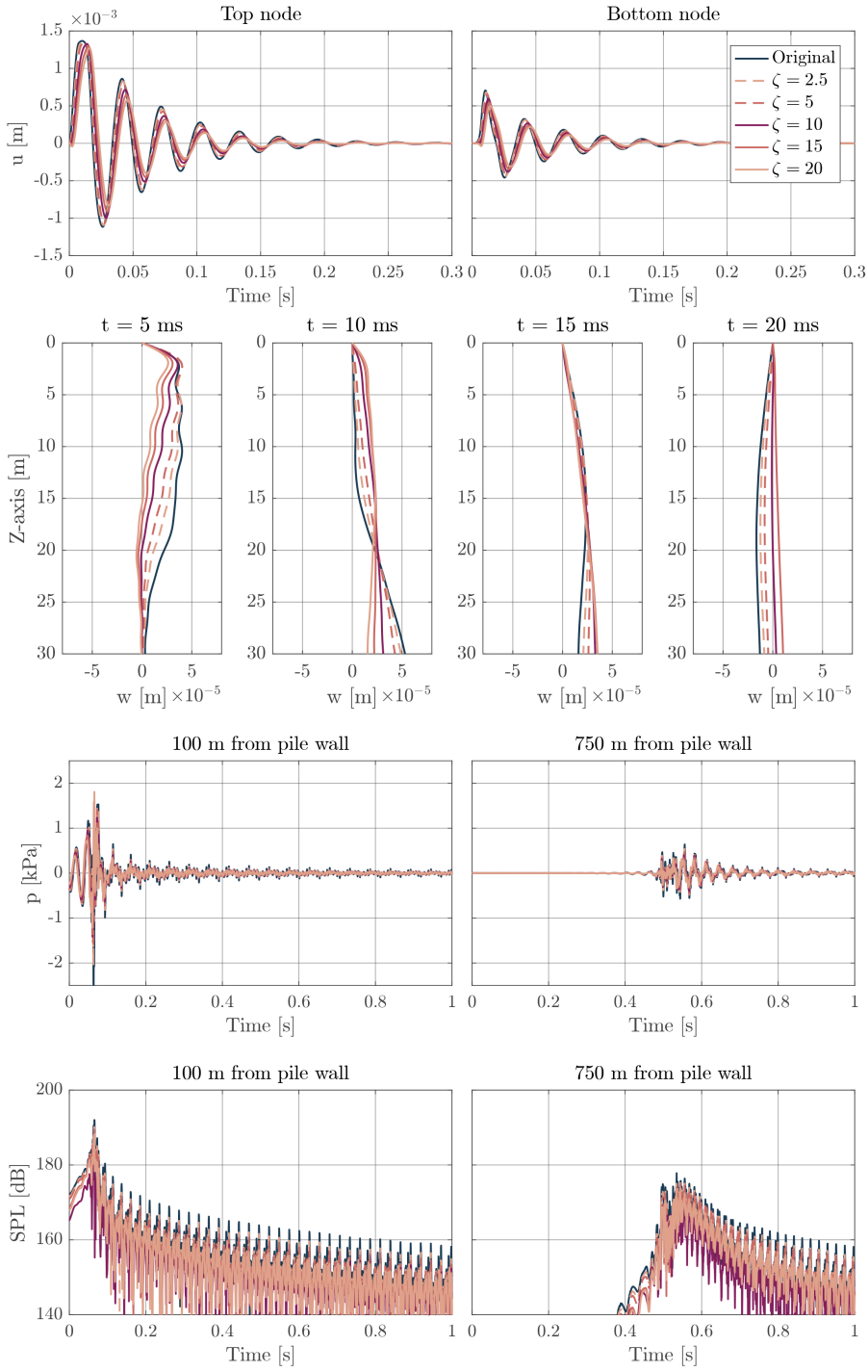

Figure 7-8: Comparison between original system and use of an oscillator with damping on longitudinal deformation, pressure levels and SPLs.

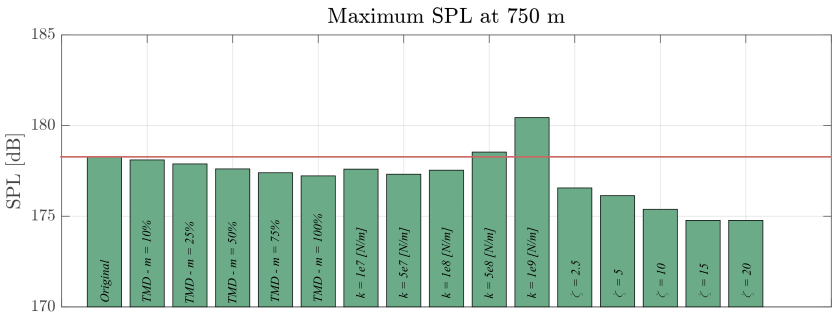

Figure 7-9: Overview of all studies in this chapter.

The second study showed that adding stiffness in combination with a TMD does not necessarily reduce the noise levels more than only using a TMD. When the stiffness is too high, the first eigenfrequency of the system increases compared to the original system and the TMD is not able to reduce the peak of this frequency unless it is tuned to the new eigenfrequency. But, when the stiffness is too low, the TMD is governing to the final noise levels, as also is seen in Figure 7-9.

Additionally, damping is investigated and although it affects a broad frequency spectrum, its results are promising. Using damping decreases amplitudes of the deformation and therefore affects pile-driveability, but it also increases the period and this combination flattens the wave front and reduces pressure and noise levels.

Chapter 8

Conclusions and recommendations

This study focused on the reduction of underwater noise, answering the following main question:

> "Is it possible for the piling of offshore monopiles to reduce generated noise, measured in the surrounding water, by changing the dynamics of the pile itself?"

This chapter will answer the main question and provide recommendations for further use of the results and for future research.

8-1 Conclusions

To be able to answer the main question, a model of a monopile under impact loading is needed. Therefore, in Chapter 2 two theories were examined to model the deformations of a pile under impact loading: a classical 1D rod and the thin shell theory. In order to obtain a simple model which provides better understanding of the physics of the pile, the monopile was modelled as a 1D rod and take into account the lateral inertia effects with Poisson's ratio. This model required an additional frequency dependent damping to avoid numerical problems around the critical frequency where the wavenumber k_p became infinity. Due to this and other simplifications described in Chapter 5, it was chosen to treat the results from this thesis as qualitative results and not quantitative results.

In order to obtain information about water pressure and underwater noise levels, the fluid pressures were simulated using the scalar velocity potential. The backwards influence of the pressure on the pile's deformation was examined in Chapter 4, where it was

concluded that the water pressure does not have a significant influence on the deformation of the pile in this model. To increase computational efficiency, it was therefore chosen to neglect the water pressure in the deformation simulations.

Finally, Chapter 6 analysed the system in order to obtain information about a way to reduce the noise generation by adding oscillators, containing mass and stiffness, around the pile. The hypothesis of using this method in reducing noise levels was that the propagating waves in the pile are constrained in radial direction and therefore the surrounding fluid's perturbation will be decreased.

The analysis consisted of two parts: first analysing the pressure intensity to investigate which frequencies have the most influence on the noise levels and then a frequency response function analysis to obtain information of these frequencies and answer the question whether or not these peaks are caused by the pile or not.

From the intensity analysis, it was concluded that two relatively low frequencies caused the most of the noise underwater. From the FRFs it was found that the first frequency was caused by the fluid as it was the cutoff frequency of the water. The frequency of the second peak was caused by the first eigenfrequency from the pile. Hence, two different causes have the biggest influence on the underwater noise levels and therefore also two different reduction approaches were needed:

- The cutoff frequency is not caused by the monopile, but adjusting the pile's structural dynamics can affect the influence of the cutoff frequency. By adding stiffness the frequency response of the longitudinal and radial deformation is expected to decrease for the frequencies up to the first eigenfrequency and therefore it is expected to reduce the intensity of the pressure at this cutoff frequency.
- By adding a TMD with the same eigenfrequency as the first eigenfrequency of the monopile, it is expected that the influence of this eigenfrequency on the noise levels is reduced due to anti-resonance at this specific eigenfrequency, without influencing other frequencies of the system.

These reduction methods were applied and its results analysed in Chapter 7. It required a new equation of motion for both the pile as the TMD. In two studies the influence of both methods are separately investigated. First the TMD reducing the first eigenfrequency of the pile is added on the bottom of the pile, using different masses and stiffnesses. It was seen that this TMD does reduce the noise levels moderately; with a mass 50% of the weight of the pile itself a reduction of approximately 0.5 dB is reached. Since the TMD is added at the bottom, the wave front of the first wave travelling down was only reduced by this TMD when it reached the bottom of the pile. Furthermore, it was seen that the amplitudes of the longitudinal deformation decreased, giving the impression that although the TMD reduces noise levels, it also reduces the pile-driveability slightly.

In the second study, the influence of stiffness on top of the pile, in order to reduce the effect of the cutoff frequency on noise levels, is analysed in combination with a

TMD with a fixed mass. This study showed that increasing stiffness, also increased the first eigenfrequency of the system. Since the first eigenfrequency of the TMD did not change, its influence decreases when stiffness increases. Additionally it was concluded from this study that a very high stiffness decreased the period and the amplitude of the deformations, leading to a higher variation in the deformations and therefore higher pressure and noise levels. Hence, adding stiffness can be used to reduce noise levels, provided that the eigenfrequency of the TMD is tuned to the new eigenfrequency of the system.

As an additional study, an oscillator containing damping was used in the system instead of a TMD and an oscillator with stiffness. Damping is assumed to reduce the amplitudes over a broader frequency spectrum and therefore it was interesting to investigate its influence on noise levels and on pile-driveability. From the results in Chapter 7 we can conclude that damping is indeed promising to use in the oscillator: it showed the most reduction in underwater noise levels of the studies perfomed in this thesis. Pile-driveability was affected though, as with the previous studies, the amplitudes of the longitudinal deformations decreased.

Finally, returning to the main question, this thesis has shown that it is possible to achieve moderate reductions in generated noise levels in the surrounding water during offshore piling, by placing oscillators on the monopile, changing the pile's dynamical characteristics.

8-2 Recommendations

This thesis gave qualitative answers to the main question and a direction in which TWD can design a new noise reduction system. However, due to simplifications and assumptions quantitative answers are left out. In order to evaluate the reduction of underwater noise levels by adding a TMD and stiffness to a monopile, it is recommended to use a 2D model to obtain more accurate results on any new design.

In this thesis the TMD was not tuned to the new eigenfrequency of the system including an oscillator with stiffness, in the second study of Chapter 7. Finding an optimal coorperation between the two oscillators, requires an extra study, where the TMD is tuned to the new eigenfrequency of the pile including extra stiffness.

Future research should also include a pile-driving analysis. Although this thesis gave promising answers on the use of oscillators to reduce underwater noise pollution and it gave a first impression on the driveability, soil characteristics and pressure waves through soil were not modelled in this thesis. Therefore, we cannot conclude what the actual influence is of adding a mass to a monopile on the driveability and a driveabiliy analysis should be performed in further research to the effects of an oscillator with mass as a noise reduction system on driveability.

In short, this thesis gave rise to a new noise reduction system. However, this system will need further research, including more quantitative results on driveability and on the actual noise reduction compared with other noise mitigation systems.

Bibliography

[1] A. Tsouvalas and A. V. Metrikine, *Underwater noise generated by offshore pile driving*. Dissertation, TU Delft, 2015.

[2] Noordzeeloket, "Beleidsnota noordzee 2016-2021," report, 2015.

[3] A. Ho, A. Mbistrova, and G. Corbetta, "The european offshore wind industry - key trends and statistics 2015," tech. rep., European Wind Energy Association, 2016.

[4] P. M. Thompson, G. D. Hastie, J. Nedwell, R. Barham, K. L. Brookes, L. S. Cordes, H. Bailey, and N. McLean, "Framework for assessing impacts of pile-driving noise from offshore wind farm construction on a harbour seal population," *Environmental Impact Assessment Review*, vol. 43, pp. 73–85, 2013.

[5] F. Thomsen, K. Ludemann, R. Kafemann, and W. Piper, "Effects of offshore windfarm noise on marine mammals and fish," report, COWRIE Ltd, 2006.

[6] H. Bailey, B. Senior, D. Simmons, R. J., G. Picken, and P. M. Thompson, "Assessing underwater noise levels during pile-driving at an offshore windfarm and its potential effects on marine mammals," *Marine Pollution Bulletin*, vol. 60, no. 3, 2010.

[7] B. L. Southall, A. E. Bowles, W. T. Ellison, Finneran, *et al.*, "Marine mammal noise exposure criteria: Initial scientific recommendations," *Aquatic mammals*, vol. 33, no. 4, p. 411, 2007.

[8] A. Tsouvalas and A. V. Metrikine, "A semi-analytical model for predicting the levels of underwater noise from offshore pile driving," *Journal of Sound and Vibration*, vol. 332, no. 13, pp. 3232–3257, 2013.

[9] B. Bruns, P. Stein, C. Kuhn, H. Sychla, and J. Gattermann, "Hydro sound measurements during the installation of large diameter offshore piles using combinations of independent noise mitigation systems," 2014.

[10] M. Fricke and R. Rolfes, "Towards a complete physically based forecast model for underwater noise related to impact pile driving," 2014.

[11] A. Norro, B. Rumes, and S. Degraer, "Differentiating between underwater construction noise of monopile and jacket foundations for offshore windmills: a case study from the belgian part of the north sea," *The Scientific World Journal*, vol. 2013, 2013.

[12] M. Jaspers Faijer, "Underwater noise caused by pile driving," report, Pondera Consult, 2014.

[13] Koninkrijk der Nederlanden, *Kavelbesluit IV windenergiegebied Borssele*, no. 14545, Staatscourant, April 2016.

[14] S. Koschinski and K. Ludemann, "Development of noise mitigation measures in offshore wind farm construction," report, 2013.

[15] G. Nehls, K. Betke, S. Eckelmann, and M. Ros, "Assessment and costs of potential engineering solutions for the mitigation of the impacts of underwater noise arising from the construction of offshore windfarms," report, 2007.

[16] M. Zampolli, M. J. J. Nijhof, C. A. F. de Jong, M. A. Ainslie, E. H. W. Jansen, and B. A. J. Quesson, "Validation of finite element computations for the quantitative prediction of underwater noise from impact pile driving," *The Journal of the Acoustical Society of America*, vol. 133, no. 1, pp. 72–81, 2013.

[17] P. Reinhal and P. Dahl, "Underwater mach wave radiation from impact pile driving: theory and observation," 2011.

[18] A. Metrikine and A. Vrouwenvelder, *Dynamics of Structures*. Delft: TU Delft, 2006.

[19] A. Love, *A treatise on the mathematical theory of elasticity*. Cambridge, at the University Press, 2nd edition ed., 1906.

[20] K. Graff, *Wave motion in elastic solids*. Dover Publications, 1991.

[21] M. Junger and D. Feit, *Sound, structures and their interaction*. MIT Press, 2nd ed., 1986.

[22] A. Deeks and M. Randolph, "Analytical modelling of hamer impact for pile driving," *International journal for numerical and analytical methods in geomechanics*, vol. 17, pp. 279–302, 1993.

[23] J. Nedwell, J. Langworthy, and D. Howell, "Assessment of sub-sea acoustic noise and vibration from offshore wind turbines and its impact on marine wildlife; initial measurements of underwater noise during construction of offshore windfarms, and comparison with background noise," report, 2003.

[24] J. Nedwell and D. Howell, "A review of offshore windfarm related underwater noise sources," 2004.

[25] A. Stokes, K. Cockrell, J. Wilson, D. Davis, and D. Warwick, "Mitigation of underwater pile driving noise during offshore construction," report, Applied Physical Science Corp., 2010.

[26] F. Jensen, W. Kuperman, M. Porter, and H. Schmidt, *Computational Ocean Acoustics*. Modern Acoustics and Signal Processing, Springer, 2011.

[27] S. Rienstra and A. Hirschberg, *An introduction to acoustics*. IWDE-Report ; 92-06, extended and revised ed., 2015.

[28] P. C. Etter, *Underwater Acoustic Modeling and Simulation*. Spon Press, 3rd ed., 2003.

[29] W. Boyce and R. DiPrima, *Elementary differential equations and boundary value problems*. Wiley, 10th edition ed., 2013.

[30] F. Jacobsen and P. Juhl, *Radiation of Sound*. 2011.

[31] A. Tsouvalas, , K. Van Dalen, and A. Metrikine, "The significance of the evanescent spectrum in structure-waveguide interaction problems," *The Journal of the Acoustical Society of America*, vol. 138, no. 4, pp. 2574–2588, 2015.

Appendix A

Rayleigh-Love equation

In this appendix, the equation of motion, described in Eq. (2-13), is elaborated using the energy method, as done in [20] and [19]. This method is based on Hamilton's equation, which states:

$$\delta \int_{t_0}^{t_1} (\tilde{K} - \tilde{P} + \tilde{W}) dt = 0 \tag{A-1}$$

Where $\tilde{K}$ is the kinetic energy density, $\tilde{P}$ is the potential energy density and $\tilde{W}$ is the work of the non-conservative forces applied on a pile.
For a rod under central axis loading, the following energy densities are given:

$$K = \frac{\rho}{2} \left(\dot{u}^2 + \dot{w}^2 \right) \tag{A-2}$$

$$P = \frac{\sigma \varepsilon}{2} \tag{A-3}$$

With

$$\dot{w} = -\nu R \frac{\partial^2 u}{\partial z \partial t} \tag{A-4}$$

Then

$$\tilde{K} = \int_V \frac{\rho}{2} \left(\dot{u}^2 + \nu^2 R^2 \left(\frac{\partial^2 u}{\partial z \partial t} \right)^2 \right) dV \tag{A-5}$$

$$\tilde{P} = \int_V \frac{\sigma \varepsilon}{2} dV \tag{A-6}$$

$$\tilde{W} = q(z,t) u \tag{A-7}$$

It is possible to integrate the previous equations over the area of the section, and since the longitudinal does not depend on other directions than the z-direction, this integral can be evaluated exactly.

$$\tilde{K} = \int_L dz \int_A \frac{\rho}{2} \left(\dot{u}^2 + \nu^2 R^2 \left(\frac{\partial^2 u}{\partial z \partial t} \right)^2 \right) dA \tag{A-8}$$

$$= \int_L \frac{\rho A}{2} \left(\dot{u}^2 + \nu^2 \frac{J}{A} \left(\frac{\partial^2 u}{\partial z \partial t} \right)^2 \right) dz \tag{A-9}$$

$$\tilde{P} = \int_L dz \int_A \frac{\sigma \varepsilon}{2} dA \tag{A-10}$$

$$= \int_L \frac{EA}{2} \left(\frac{\partial u}{\partial z} \right)^2 dz \tag{A-11}$$

This results in the following Hamilton's equation:

$$\delta \int_{t_0}^{t_1} dt \int_L A \left[\frac{\rho}{2} \left(\dot{u}^2 + \nu^2 \frac{J}{A} \left(\frac{\partial^2 u}{\partial z \partial t} \right)^2 \right) - \frac{E}{2} \left(\frac{\partial u}{\partial z} \right)^2 + q(z,t) u \right] dz = 0 \tag{A-12}$$

Let's state the following:

$$I = \int \int G \left(z, t, u, \frac{\partial u}{\partial z}, \frac{\partial u}{\partial z}, \frac{\partial^2 u}{\partial z \partial t} \right) + q u dz dt \tag{A-13}$$

Where

$$G = \frac{\rho A}{2} \left(\dot{u}^2 + \nu^2 \frac{J}{A} \left(\frac{\partial^2 u}{\partial z \partial t} \right)^2 \right) - \frac{EA}{2} \left(\frac{\partial u}{\partial z} \right)^2 \tag{A-14}$$

Then the variation of the integral I is equal to:

$$\delta I = \int_t \int_L \left(\frac{\partial G}{\partial u_z} \delta u_z + \frac{\partial G}{\partial \dot{u}} \delta \dot{u} + \frac{\partial G}{\partial \dot{u}_z} \delta \dot{u}_z + q \delta u \right) dz dt = 0 \tag{A-15}$$

Where each part of the integral can be obtained by integration by parts:

$$\int_{t_0}^{t_1} \int_L \frac{\partial G}{\partial u_z} \delta u_z dz dt = \int_{t_0}^{t_1} dt \left\{ \frac{\partial G}{\partial u_z} \delta u |_L - \int_L \frac{\partial}{\partial z} \left(\frac{\partial G}{\partial u_z} \right) \delta u dz \right\} \tag{A-16}$$

$$\int_{t_0}^{t_1}\int_L \frac{\partial G}{\partial \dot{u}}\delta\dot{u}dzdt = \int_L dz\left\{\frac{\partial G}{\partial \dot{u}}\delta u|_{t_0}^{t_1} - \int_{t_0}^{t_1}\frac{\partial}{\partial t}\left(\frac{\partial F}{\partial \dot{u}}\right)\delta u dt\right\} \tag{A-17}$$

$$\begin{aligned}\int_{t_0}^{t_1}\int_L \frac{\partial G}{\partial \dot{u}_z}\delta\dot{u}_z dzdt &= \int_{t_0}^{t_1} dt\frac{\partial G}{\partial \dot{u}_z}\delta\dot{u}|_L \\ &\quad - \int_L dz\left\{\frac{\partial}{\partial z}\left(\frac{\partial G}{\partial \dot{u}_z}\right)\delta u|_{t_0}^{t_1} - \int_{t_0}^{t_1}\frac{\partial^2}{\partial z\partial t}\left(\frac{\partial G}{\partial \dot{u}_z}\right)\delta u dt\right\} \\ &= \frac{\partial G}{\partial \dot{u}_z}\delta u\Big|_L\Big|_{t_0}^{t_1} - \int_{t_0}^{t_1}\frac{\partial}{\partial t}\left(\frac{\partial G}{\partial \dot{u}_z}\right)\delta u\Big|_L dt \\ &\quad - \int_L dz\left\{\frac{\partial}{\partial z}\left(\frac{\partial G}{\partial \dot{u}_z}\right)\delta u\Big|_{t_0}^{t_1} - \int_{t_0}^{t_1}\frac{\partial^2}{\partial z\partial t}\left(\frac{\partial G}{\partial \dot{u}_z}\right)\delta u dt\right\}\end{aligned} \tag{A-18}$$

This results in the following:

$$\delta I = \int_{t_0}^{t_1}\int_L\left(-\frac{\partial}{\partial z}\left(\frac{\partial G}{\partial u_z}\right) - \frac{\partial}{\partial t}\left(\frac{\partial G}{\partial \dot{u}} + q\delta u\right) + \frac{\partial^2}{\partial z\partial t}\left(\frac{\partial G}{\partial \dot{u}_z}\right)\right)\delta u dzdt \tag{A-19}$$

$$+ \int_{t_0}^{t_1}\left(\frac{\partial G}{\partial u_z} - \frac{\partial}{\partial t}\left(\frac{\partial G}{\partial \dot{u}_z}\right)\right)\delta u\Big|_L \tag{A-20}$$

$$+ \int_L\left(\frac{\partial G}{\partial \dot{u}} - \frac{\partial}{\partial z}\left(\frac{\partial G}{\partial \dot{u}_z}\right)\right)\delta u\Big|_{t_0}^{t_1} + \frac{\partial G}{\partial \dot{u}_z}\delta u\Big|_L\Big|_{t_0}^{t_1} = 0 \tag{A-21}$$

Assuming that the system starts from equilibrium at $t = t_0$ and reaches equilibrium at $t = t_1$, one can say that $\delta u(z, t_0) = \delta u(z, t_1) = 0$ (hence, initial conditions are introduced here) and therefore $\delta u|_{t_0}^{t_1} = 0$.

This leaves us the following:

$$\delta I = \int_{t_0}^{t_1}\int_L\left(-\frac{\partial}{\partial z}\left(\frac{\partial G}{\partial u_z}\right) - \frac{\partial}{\partial t}\left(\frac{\partial F}{\partial \dot{u}}\right) + \frac{\partial^2}{\partial z\partial t}\left(\frac{\partial G}{\partial \dot{u}_z}\right) + q\delta u\right)\delta u dzdt \tag{A-22}$$

$$+ \int_{t_0}^{t_1}\left(\frac{\partial G}{\partial u_z} - \frac{\partial}{\partial t}\left(\frac{\partial G}{\partial \dot{u}_z}\right)\right)\delta u\Big|_L = 0 \tag{A-23}$$

The first line gives the equation of motion, while from the second line the boundary conditions can be obtained:

$$\int_t\int_L\left\{-\frac{\partial}{\partial zx}\left(\frac{\partial G}{\partial u_z}\right) - \frac{\partial}{\partial t}\left(\frac{\partial G}{\partial \dot{u}}\right) + \frac{\partial^2}{\partial z\partial t}\left(\frac{\partial G}{\partial \dot{u}}\right) + q\right\}\delta u dzdt = 0 \tag{A-24}$$

Where the equation within the integral gives the Euler equation:

$$\frac{\partial}{\partial z}\left(\frac{\partial G}{\partial u_z}\right)+\frac{\partial}{\partial t}\left(\frac{\partial G}{\partial \dot{u}}\right)-\frac{\partial^2}{\partial z \partial t}\left(\frac{\partial G}{\partial \dot{u}}\right)+q(z,t)=0 \tag{A-25}$$

When substituting Eq. (A-14) into the above equation, the result is the equation of motion by Love:

$$c^2\frac{\partial^2 u}{\partial z^2}-\frac{\partial^2 u}{\partial t^2}+\frac{\nu^2 J}{A}\frac{\partial^2}{\partial t^2}\left(\frac{\partial^2 u}{\partial z^2}\right)+q(z,t)=0 \tag{A-26}$$

Leaving the second line, which results in the boundary conditions:

$$\int_{t_0}^{t_1}\left(\frac{\partial G}{\partial u_z}-\frac{\partial}{\partial t}\left(\frac{\partial G}{\partial \dot{u}_z}\right)\right)\delta u\Big|_L dt=0 \tag{A-27}$$

There are two options:

$$z=0,L \qquad \frac{\partial G}{\partial u_z}-\frac{\partial}{\partial t}\left(\frac{\partial G}{\partial \dot{u}_z}\right)=0 \tag{A-28}$$

$$\delta u=0 \tag{A-29}$$

For this case it is convenient that u will not be zero, for each z and therefore:

$$z=0,L \qquad \frac{\partial G}{\partial u_z}-\frac{\partial}{\partial t}\left(\frac{\partial G}{\partial \dot{u}_z}\right)=0 \tag{A-30}$$

$$EA\frac{\partial u}{\partial z}+\rho A\frac{\nu^2 J}{A}\frac{\partial}{\partial t}\left(\frac{\partial^2 u}{\partial z \partial t}\right)=0 \tag{A-31}$$

$$c^2\frac{\partial u}{\partial z}+\frac{\nu^2 J}{A}\frac{\partial^3 u}{\partial z \partial t^2}=0 \tag{A-32}$$

Appendix B

Derivation of the boundary conditions

Continuing the last appendix here, one important note has to be made on the application of external forces. When the external forces are only applied on the boundaries, it is possible to use these forces as boundary conditions. For the case in this research this is very convenient, since both the impact force and the forces due to the spring and dashpot are applied only at the top and bottom respectively.

The Hamilton's equation found in Appendix A equals:

$$\delta I = \int_{t_0}^{t_1} \int_L \left(-\frac{\partial}{\partial z}\left(\frac{\partial G}{\partial u_z}\right) - \frac{\partial}{\partial t}\left(\frac{\partial F}{\partial \dot{u}}\right) + \frac{\partial^2}{\partial z \partial t}\left(\frac{\partial G}{\partial \dot{u}_z}\right) + q\delta u \right) \delta u dz dt \tag{B-1}$$

$$+ \int_{t_0}^{t_1} \left(\frac{\partial G}{\partial u_z} - \frac{\partial}{\partial t}\left(\frac{\partial G}{\partial \dot{u}_z}\right) \right) \delta u \Big|_L \tag{B-2}$$

Now, for the current case there are two external forces introduced:

$$z = 0 \qquad -F(z,t)\delta(z) \tag{B-3}$$

$$z = L \qquad -\left(k_d u(z,t) + c_d \dot{u}(z,t)\right)\delta(z-L) \tag{B-4}$$

The Dirac-delta function gives two options here, either leave the external forces in the equation of motion, or integrate along z and use them in the boundary conditions. Both cases will be further elaborated in the following two sections.

B-1 Case 1 - External forces in equation of motion

As stated in the previous Appendix, the equation in the first integral gives the Euler equation:

$$\frac{\partial}{\partial z}\left(\frac{\partial G}{\partial u_z}\right)+\frac{\partial}{\partial t}\left(\frac{\partial G}{\partial \dot{u}}\right)-\frac{\partial^2}{\partial z \partial t}\left(\frac{\partial G}{\partial \dot{u}}\right)-F(z,t)\delta(z)-\left(k_d u(z,t)-c_d \dot{u}(z,t)\right)\delta(z-L)=0 \tag{B-5}$$

When substituting Eq. (A-14) into the above equation, the result is the equation of motion:

$$c^2\frac{\partial^2 u}{\partial z^2}-\frac{\partial^2 u}{\partial t^2}+\frac{\nu^2 J}{A}\frac{\partial^2}{\partial t^2}\left(\frac{\partial^2 u}{\partial z^2}\right)+F(z,t)\delta(z)+\left(k_d u(z,t)+c_d \dot{u}(z,t)\right)\delta(z-L)=0 \tag{B-6}$$

Leaving the second line, which results in the boundary conditions, as elaborated in the previous section and resulting in:

$$z=0,L \qquad\qquad c^2\frac{\partial u}{\partial z}+\frac{\nu^2 J}{A}\frac{\partial^3 u}{\partial z \partial t^2}=0 \tag{B-7}$$

B-2 Case 2 - External forces in boundary conditions

In the second case the external forces will be integrated over the full length of the pile, resulting in the following Hamilton's equation:

$$\delta I=\int_{t_0}^{t_1}\int_L\left(-\frac{\partial}{\partial z}\left(\frac{\partial G}{\partial u_z}\right)-\frac{\partial}{\partial t}\left(\frac{\partial G}{\partial \dot{u}}\right)+\frac{\partial^2}{\partial z \partial t}\left(\frac{\partial G}{\partial \dot{u}_z}\right)\delta u\right)\delta u dz dt \tag{B-8}$$

$$+\int_{t_0}^{t_1}\left(\frac{\partial G}{\partial u_z}-\frac{\partial}{\partial t}\left(\frac{\partial G}{\partial \dot{u}_z}\right)-F(z,t)\delta(z)-\left(k_d u(z,t)-c_d \dot{u}(z,t)\right)\delta(z-L)\right)\delta u\Big|_L \tag{B-9}$$

Then, the final equation of motion is equal to the equation of motion by Love:

$$c^2\frac{\partial^2 u}{\partial z^2}-\frac{\partial^2 u}{\partial t^2}+\frac{\nu^2 J}{A}\frac{\partial^2}{\partial t^2}\left(\frac{\partial^2 u}{\partial z^2}\right)=0 \tag{B-10}$$

Leaving the equations for the boundary conditions:

$$\left(\frac{\partial G}{\partial u_z} - \frac{\partial}{\partial t}\left(\frac{\partial G}{\partial \dot{u}_z}\right) - F(t)\delta(z) - \left(k_d u(z,t) - c_d \dot{u}(z,t)\right)\delta(z-L)\right)\delta u\Big|_L = 0 \qquad \text{(B-11)}$$

As it is a trivial solution to assume δu is zero for each point along the z-axis, the following condition has to be met:

$$z = 0 \qquad \frac{\partial G}{\partial u_z} - \frac{\partial}{\partial t}\left(\frac{\partial G}{\partial \dot{u}_z}\right) - F(t) = 0 \quad \rightarrow \qquad \text{(B-12)}$$

$$EA\frac{\partial u}{\partial z} + \rho A\frac{\nu^2 J}{A}\frac{\partial}{\partial t}\left(\frac{\partial^2 u}{\partial z \partial t}\right) + F(t) = 0 \quad \rightarrow \qquad \text{(B-13)}$$

$$c^2\frac{\partial u}{\partial z} + \frac{\nu^2 J}{A}\frac{\partial}{\partial t}\left(\frac{\partial^2 u}{\partial z \partial t}\right) = -\frac{F(t)}{\rho A} \qquad \text{(B-14)}$$

$$z = L \qquad \frac{\partial G}{\partial u_z} - \frac{\partial}{\partial t}\left(\frac{\partial G}{\partial \dot{u}_z}\right) - \left(k_d u(L,t) + c_d \dot{u}(L,t)\right) = 0 \quad \rightarrow \qquad \text{(B-15)}$$

$$EA\frac{\partial u}{\partial z} + \rho A\frac{\nu^2 J}{A}\frac{\partial}{\partial t}\left(\frac{\partial^2 u}{\partial z \partial t}\right) + \left(k_d u(L,t) + c_d \dot{u}(L,t)\right) = 0 \quad \rightarrow \qquad \text{(B-16)}$$

$$c^2\frac{\partial u}{\partial z} + \frac{\nu^2 J}{A}\frac{\partial}{\partial t}\left(\frac{\partial^2 u}{\partial z \partial t}\right) = -\left(\frac{k_d}{\rho A}u(L,t) + \frac{c_d}{\rho A}\dot{u}(L,t)\right) \qquad \text{(B-17)}$$

Appendix C

Derivation of coupled equation of motion

In this Appendix the coupled equation of motion is elaborated using the energy method, the same method as used in Appendix A. The difference with the previous Appendix is the potential energy, which now also includes the pressure from the fluid.

For a rod under central axis loading and under pressure perpendicular to the central axis, the following energy densities are given:

$$K = \frac{\rho}{2}\left(\dot{u}^2 + \dot{w}^2\right) \tag{C-1}$$

$$P = \frac{\sigma\varepsilon}{2} + \nu p u(z,t) \tag{C-2}$$

With

$$\dot{w} = -\nu R \frac{\partial^2 u}{\partial z \partial t} \tag{C-3}$$

Then

$$\tilde{K} = \int_L dz \int_A \frac{\rho}{2}\left(\dot{u}^2 + \nu^2 R^2 \left(\frac{\partial^2 u}{\partial z \partial t}\right)^2\right) dA \tag{C-4}$$

$$= \int_L \frac{\rho A}{2}\left(\dot{u}^2 + \nu^2 \frac{J}{A}\left(\frac{\partial^2 u}{\partial z \partial t}\right)^2\right) dz \tag{C-5}$$

$$\tilde{P} = \int_L dz \int_A \left(\frac{\sigma\varepsilon}{2} + \nu p u \right) dA \tag{C-6}$$

$$= \int_L A \left(\frac{E}{2} \left(\frac{\partial u}{\partial z} \right)^2 + \nu p u \right) dz \tag{C-7}$$

This results in the following Hamilton's equation:

$$\delta \int_{t_0}^{t_1} dt \int_L A \left[\frac{\rho}{2} \left(\dot{u}^2 + \nu^2 \frac{J}{A} \left(\frac{\partial^2 u}{\partial z \partial t} \right)^2 \right) - \frac{E}{2} \left(\frac{\partial u}{\partial z} \right)^2 \nu p u \right] dz = 0 \tag{C-8}$$

Let's state the following:

$$I = \int \int \left\{ G \left(z, t, \frac{\partial u}{\partial z}, \frac{\partial u}{\partial z}, \frac{\partial^2 u}{\partial z \partial t} \right) + \nu p u \right\} dz dt \tag{C-9}$$

Where

$$G = \frac{\rho A}{2} \left(\dot{u}^2 + \nu^2 \frac{J}{A} \left(\frac{\partial^2 u}{\partial z \partial t} \right)^2 \right) - \frac{EA}{2} \left(\frac{\partial u}{\partial z} \right)^2 \tag{C-10}$$

Then the variation of the integral I is found, following the same procedure as in Appendix A:

$$\int_t \int_L \left\{ -\frac{\partial}{\partial z} \left(\frac{\partial F}{\partial u_z} \right) - \frac{\partial}{\partial t} \left(\frac{\partial F}{\partial \dot{u}} \right) + \frac{\partial^2}{\partial z \partial t} \left(\frac{\partial F}{\partial \dot{u}} \right) + \nu p \right\} \delta u dz dt = 0 \tag{C-11}$$

Where the equation within the integral gives the Euler equation:

$$\frac{\partial}{\partial z} \left(\frac{\partial F}{\partial u_z} \right) + \frac{\partial}{\partial t} \left(\frac{\partial F}{\partial \dot{u}} \right) - \frac{\partial^2}{\partial z \partial t} \left(\frac{\partial F}{\partial \dot{u}} \right) + \nu p = 0 \tag{C-12}$$

Substituting Eq. (C-10) into the above equation, gives the final equation of motion of the coupled system:

$$c^2 \frac{\partial^2 u}{\partial z^2} - \frac{\partial^2 u}{\partial t^2} + \frac{\nu^2 J}{A} \frac{\partial^2}{\partial t^2} \left(\frac{\partial^2 u}{\partial z^2} \right) + \frac{\nu}{\rho} p = 0 \tag{C-13}$$